

A *SPITZER* VIEW OF THE YOUNG OPEN CLUSTER NGC 2264

HWANKYUNG SUNG^{1,4}, JOHN R. STAUFFER², AND MICHAEL S. BESSELL³

¹ Department of Astronomy and Space Science, Sejong University, Kunja-dong 98, Kwangjin-gu, Seoul 143-747, Korea; sungh@sejong.ac.kr

² Spitzer Science Center, California Institute of Technology, 314-6, Pasadena, CA 91125, USA; stauffer@ipac.caltech.edu

³ Research School of Astronomy and Astrophysics, Australian National University, MSO, Cotter Road, Weston, ACT 2611, Australia; bessell@mso.anu.edu.au

Received 2009 January 20; accepted 2009 June 15; published 2009 September 4

ABSTRACT

We have performed mid-IR photometry of the young open cluster NGC 2264 using the images obtained with the *Spitzer Space Telescope* Infrared Array Camera and Multiband Imaging Photometer for *Spitzer* instruments and presented a normalized classification scheme of young stellar objects in various color–color diagrams to make full use of the information from multicolor photometry. These results are compared with the classification scheme based on the slope of the spectral energy distribution (SED). From the spatial distributions of Class I and II stars, we have identified two subclustering of Class I objects in the CONE region of Sung et al. The disked stars in the other star-forming region S Mon are mostly Class II objects. These three regions show a distinct difference in the fractional distribution of SED slopes as well as the mean value of SED slopes. The fraction of stars with primordial disks is nearly flat between $\log m = 0.2$ and -0.5 and that of transition disks is very high for solar mass stars. In addition, we have derived a somewhat higher value of the primordial disk fraction for NGC 2264 members located below the main pre-main-sequence locus (so-called BMS stars). This result supports the idea that BMS stars are young stars with nearly edge-on disks. We have also found that the fraction of primordial disks is very low near the most massive star S Mon and increases with distance from S Mon.

Key words: open clusters and associations: individual (NGC 2264) – planetary systems: protoplanetary disks – stars: formation – stars: pre-main sequence

Online-only material: color figures, machine-readable table and VO table

1. INTRODUCTION

Curiosity about the formation of stars and planets is fundamental to mankind. The hypothesis of planet formation in the protosolar nebula can be traced back to the eighteenth century. Despite good theoretical support for the existence of disks around young stars (Lynden-Bell & Pringle 1974), they were largely ignored for many years because the existing observational data could be explained without reference to disks (Sung et al. 2007). This situation changed slowly over time, particularly as IR detectors became sensitive to the warm dust component of circumstellar disks (Strom et al. 1989; Lada & Wilking 1984). The Two Micron All Sky Survey (2MASS; Skrutskie et al. 2006) provided an unprecedented amount of data in the near-IR passbands that were used in many important studies, such as the distribution of embedded star-forming regions (SFRs), statistical estimates of young stellar objects (YSOs), and the general distribution of stars in the Galaxy. However in the earliest stages of star formation, the spectral energy distributions (SEDs) were dominated by radiation from circumstellar dust at mid-IR and far-IR wavelengths, with little at near-IR wavelengths of the 2MASS.

The launch of the *Spitzer Space Telescope* revolutionized the study of star formation. Infrared Array Camera (IRAC; Fazio et al. 2004) and Multiband Imaging Photometer for *Spitzer* (MIPS; Rieke et al. 2004) instrument teams and several Legacy projects obtained observations of young open clusters and individual young SFRs, including “From Molecular Cores to Planet-Forming Cores (c2d)” (Evans et al. 2003), “Formation and Evolution of Planetary Systems (FEPS)” (Carpenter et al. 2009), “Taurus—The *Spitzer* Map of the Taurus Molecular Clouds”

(Padgett et al. 2007), and “Gould’s Belt—Star Formation in the Solar Neighborhood” (Allen et al. 2007a), providing a greatly improved census and characterization of young stars and their disks in a wide range of star-forming environments.

As an example of the breadth of these surveys, the c2d project aimed to survey with IRAC and MIPS five nearby star-forming clouds within a certain reddening boundary and to produce catalogs and SEDs for YSO members over the entire SFR (i.e., not spatially biased to only the cloud cores). IRAC and MIPS instrument teams surveyed relatively distant young open clusters and OB associations under Guaranteed Time Observation (GTO) programs, for example, IC 348 (Lada et al. 2006), NGC 2264 (Teixeira et al. 2006; Young et al. 2006), σ Ori (Hernández et al. 2007a), Cep OB2 (Sicilia-Aguilar et al. 2006), etc. Many scientific papers have already been published from these projects. Amongst them, Harvey et al. (2007) studied the YSOs in the Serpens cloud and found that disks in less evolved stages were more clustered. Gutermuth et al. (2008) also found a different spatial distribution of Class I and II objects in NGC 1333. Class I objects in NGC 1333 were located along the filament, while Class II objects were more widely distributed. Recently, Cieza et al. (2007) studied the disk properties of a specific type of stars—weak-line T Tauri Stars (WTTSs). Many investigators have previously derived the overall fraction of primordial disks⁵ around YSOs in young open clusters and groups (Dahm & Hillenbrand 2007; Hernández et al. 2008; Megeath et al. 2005) and tried to determine the lifetime of primordial disks to constrain the planet-building timescale. Although many attempts have been made to determine the effects of massive stars on disk evolution, little evidence has been found.

⁴ Visiting Associate, Spitzer Science Center, California Institute of Technology, 314-6, Pasadena, CA 91125, USA.

⁵ The primordial disk is defined as the disks around a YSO resulting from the star formation process—Class I and II objects.

The core cluster of the Mon OB1 association, NGC 2264, is one of the most studied young open clusters. Although the cluster is more distant than the Orion nebula cluster (ONC), NGC 2264 is still relatively nearby and serves as a good prototypical populous, young open cluster ($d \approx 760$ pc; Sung et al. 1997). In addition, the large number (about 1000) of known pre-main-sequence (PMS) members and nearly zero foreground reddening has attracted many observational studies from radio to X-ray wavelengths. In this section, we will summarize the most relevant studies only (see Dahm 2008 for an extensive review of NGC 2264). Allen (1972) discovered a strong mid-IR source in NGC 2264 (IRS1). Later, Harvey et al. (1977) observed this object with the NASA G. P. Kuiper Airborne Observatory in the far-IR and suggested that it might be a stellar or protostellar object of a moderate mass, $\sim 5\text{--}10 M_{\odot}$. Margulis et al. (1989) studied the Mon OB1 (NGC 2264) molecular clouds with *IRAS* 12 μm , 25 μm , 60 μm , and 100 μm images and found 30 discrete far-IR sources. They also calculated the spectral index of these sources and found that 18 *IRAS* sources were Class I objects. They concluded that star formation is ongoing in NGC 2264. From the *K*-band luminosity function, Lada et al. (1993) estimated the number of cluster members to be 360 ± 130 . Rebull et al. (2002) performed an optical and near-IR survey of the cluster, presenting photometry for over 5600 stars. They used various disk and mass accretion indicators and derived an inner disk fraction ranging from 21% to 56% depending on the empirical disk indicator that was used, and a typical mass accretion rate on the order of $10^{-8} M_{\odot} \text{ yr}^{-1}$. Recently, Teixeira et al. (2006), using mid-IR images obtained with the *Spitzer Space Telescope*, found a dense embedded mini-cluster (Spokes cluster) around the strong IR source IRS2 in NGC 2264. They found uniformly spaced protostars in a semi-linear fashion. Based on the fact that the distance between the nearest protostars was of the order of the Jeans length, they concluded that this geometry was evidence for thermal fragmentation. Young et al. (2006) studied the SED of objects around IRS2 and confirmed the youth of these objects. Sung et al. (2008) published a vast amount of optical photometric data for NGC 2264. From the surface density distribution of $\text{H}\alpha$ emission stars, they identified two dense SFRs (S MON and CONE) and a HALO region surrounding the two SFRs.

In this paper, we present the overall properties of NGC 2264 in the mid-IR passbands. The data from this work will be used in a future paper on the initial mass function and young brown dwarf candidates in NGC 2264. We will describe the photometry from *Spitzer* images in Section 2. Along with the mid-IR photometric data for about 22,000 objects, optical and 2MASS counterparts of these mid-IR sources will be identified. In addition the X-ray and $\text{H}\alpha$ emission stars in mid-IR color-color (C-C) diagrams will be presented in this section. The classification scheme used in this study is described and compared with previous methods in Section 3. The mid-IR color-magnitude diagrams (CMDs) and the optical CMD of stars detected in the mid-IR photometry will also be presented in this section. In Section 4, we will identify two young subclustering including the Spokes cluster from the spatial distribution of Class I sources and show the fractional distribution of the SED slope of YSOs in each subclustering. The fraction of disked stars will be derived in Section 5 and the effect of massive stars on primordial disks will be examined in Section 6. The disk fraction of below the PMS locus (so-called BMS) stars will be discussed in Section 7. The mid-IR characteristics of several interesting objects are also discussed in this section. The summary of this work is given in Section 8.

2. OBSERVATION AND DATA REDUCTION

2.1. *Spitzer* Observations of NGC 2264

The *Spitzer* mapping observations were performed under program ID 37 (PI: G. Fazio) in 7×11 mosaics. Each pointing was imaged in the high dynamic range mode (exposure time: 0.4 s and 10.4 s). The mapping of NGC 2264 was performed on 2004 March 6 and October 8, with a different spacecraft position angle at the two epochs. Two iterations each day were made with an offset of about 12 arcsec. The observed region is slightly larger than the HALO region defined in Sung et al. (2008). The Astronomical Observation Requests (AORs) utilized for these maps were numbers 3956480, 3956736, 3956992, and 3957248.

MIPS scanning of NGC 2264 was obtained on 2004 March 16 (PID 58) at the medium scan rate (exposure time: 3.67 s). Fourteen scans of 0:75 length, with 160'' offsets, were used. The observed area is larger and fully covered the region observed with IRAC. The AOR utilized for the MIPS mapping was number 4317184. The post-BCD (basic calibrated and mosaiced) images were downloaded from the *Spitzer* archive. The pixel size of the IRAC post-BCD data is $1''.2 \times 1''.2$, while that of the MIPS 24 μm data is $2''.45 \times 2''.45$. The data utilized pipeline processing software version S14.0.0 for the IRAC images and S16.1.0 for the MIPS 24 μm image.

2.2. Photometry

We have used the IRAF⁶ version of DAOPHOT to derive point-spread function (PSF)-fitting photometry for stars in the field of NGC 2264. Because *Spitzer* IRAC images are undersampled, PSF fitting yields photometry with relatively poor signal-to-noise. For uncrowded fields with little nebulosity, aperture photometry would provide photometry with lower noise than PSF-fitting photometry for IRAC data. However, portions of the NGC 2264 field are crowded, or have highly variable and strong nebulosity, or both. We believe that the PSF-fitting photometry provides a more uniform and reliable photometry for the entire set of cluster stars, admittedly at the expense of having more noise than aperture photometry for the stars where the backgrounds are benign and crowding is not an issue. For most stars in the cluster, because we have four independent sets of data, the PSF-fitting photometric accuracy is improved by averaging the results from the separate AORs.

To minimize the contribution of the spatially varying nebulosity, we used a very small fitrad of DAOPHOT parameter (1.4 pixels) and then corrected to 3 pixel radii magnitudes using the magnitude differences at the two radii calculated from bright stars free of nebulosity. The sky background was taken from the annulus between 3 and 7 pixels from the source. As post-BCD images are calibrated, resampled, and mosaiced data, the spatial variation inherent in the original BCD images is altered and removed. For this reason, we assumed that there is no spatial variation in the PSF for post-BCD images, that is, set the "varorder" parameter in daopars to "0."

The post-BCD mosaic images are flux calibrated in units of MJy sr^{-1} . The photometric zero points to use for the PHOT module of DAOPHOT were calculated using the pixel scale and the flux of a zeroth magnitude star from the IRAC Handbook. The values used were 17.30, 16.82, 16.33, and 15.69 mag for channels 1 through 4, respectively. The aperture corrections

⁶ IRAF is distributed by the National Optical Astronomy Observatory, which is operated by the Association of Universities for Research in Astronomy, Inc., under cooperative agreement with the National Science Foundation.

(to an aperture = 10 pixels, sky annulus = 10–20 pixels) applied were -0.127 , -0.130 , -0.145 , and -0.228 mag for channels 1 through 4, respectively. Hora et al. (2008) gave slightly different aperture corrections for post-BCD images, but the differences are less than 0.015 mag that has a negligible effect on determining the physical properties for our stars. As MIPS $24\ \mu\text{m}$ images are well-sampled data, PSF photometry for them is rather straightforward. We used a 2.4 pixel FIT radius and $20''\text{--}32''$ for the sky annuli. The post-BCD images were calibrated in units of MJy sr^{-1} and it was $141.1\ \mu\text{Jy pixel}^{-2}$ for MIPS $24\ \mu\text{m}$ images. The photometric zero point to be used with PHOT (11.76 mag) was calculated using the pixel scale and the flux of a zeroth magnitude star in the MIPS Handbook (7.14 Jy). The final $24\ \mu\text{m}$ magnitudes [24] were obtained by applying an aperture correction of -0.52 mag.

It is worth mentioning two points relating to the photometry. The first concerns the detection and removal of cosmic rays. Because the IRAC images are undersampled, it is very difficult to distinguish cosmic rays from point sources. We used the fact that we have multiple, independent mosaics of the cluster to eliminate cosmic rays not removed within an individual AOR by the MOPEX mosaicing software. That is, we created catalogs of all point-like sources for each AOR. When we combined the four catalogs, we rejected all sources that were identified only in a single AOR.

The second point concerns point source photometry in spatially varying nebulosity. In order to help eliminate false point sources that are in fact knots or edges in the nebula, we created median-subtracted mosaic images. We visually examined these median-subtracted images for all the point sources in our master catalog that lie within the nebular regions and deleted all sources that do not appear point like in the median-subtracted images. Our final photometry was however still performed on the original mosaic images.

We present the photometric data from four IRAC bands and the MIPS $24\ \mu\text{m}$ band for 21,991 objects in Table 1. We label the objects in Table 1 as SST + the identification number in the first column. The total number of objects detected from the photometry are 21,224, 18,329, 5113, 2302, and 506 in the $3.6\ \mu\text{m}$, $4.5\ \mu\text{m}$, $5.8\ \mu\text{m}$, $8.0\ \mu\text{m}$, and $24\ \mu\text{m}$ bands, respectively. The weighted mean values and weighted errors of the magnitude from multiple observations were calculated as in Sung & Lee (1995) (weight = $1/\epsilon^2$). The distribution of photometric errors is shown in Figure 1. The distribution of photometric errors in [24] is the typical distribution of errors from the PSF photometry of well-sampled data. For undersampled data, such as the IRAC or *Hubble Space Telescope*/Wide Field Planetary Camera 2 (*HST*/WFPC2) images, the distribution is far different—the photometric errors are no better than 0.1 mag even for bright stars (see the error distribution of bright stars detected only in the short exposure images in Figure 4). But as four epochs of data with two exposure times per epoch are available, there could be a maximum number of eight detections for some objects. If the magnitudes from all images are consistent, the resulting final error is small. If not, the resulting error will be larger. Such a trend can be seen in Figure 1—there are many faint stars with small errors.

Due to the lower spatial resolution of the MIPS $24\ \mu\text{m}$ data, we paid considerable attention to finding the appropriate IRAC counterparts. If two or more IRAC sources were matched as counterparts of a [24] source (matching radii = $2''.5$), we applied the following rule for the [24] magnitude. If neither of them showed any evident IRAC excess, then the [24] flux was

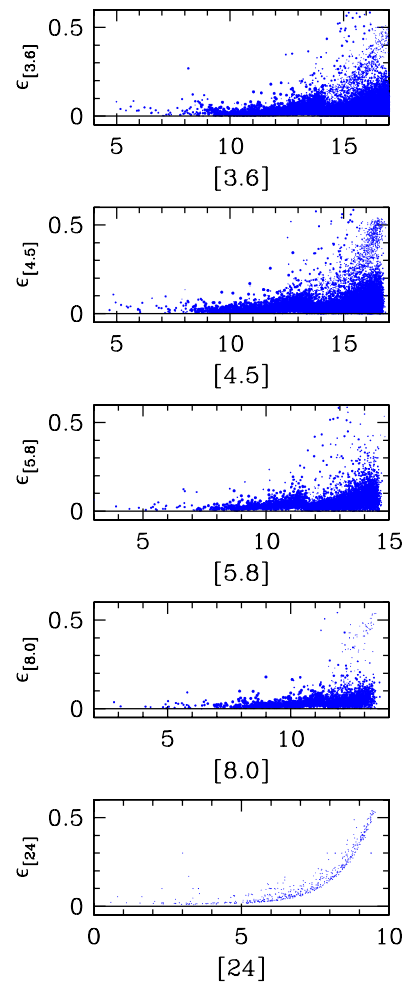


Figure 1. Distribution of photometric errors as a function of magnitude. The size of symbols are proportional to the number of observations. (A color version of this figure is available in the online journal.)

assigned to the nearest object (2 cases out of 18). If only one source showed a certain or probable IRAC excess (9 cases), then the [24] flux was assigned to that IR excess star. For one case, although both objects showed an IRAC excess, we assigned the MIPS flux to only one of them because that source was much brighter than the other. In four cases, more than one IRAC source of similar brightness showed an IR excess. For such cases we drew a wavelength versus brightness plot, extrapolated to $24\ \mu\text{m}$, and then determined the brightness difference at $24\ \mu\text{m}$. Using this difference and measured [24] flux, we derived an estimated [24] magnitude for each component. In the extrapolation, we assumed a logarithmic function-like variation for Class II stars and a cubic function-like variation for Class I objects. For these objects, we assigned a large error of -0.1 mag if the two objects were of similar brightness or 0.3 mag if the brightness difference was large (see the lowest panel of Figure 1). For two cases, because both objects are very faint in [3.6] and [4.5] and not detected in [5.8] and [8.0], the [24] flux was not assigned to either of them.

We compared our data with Young et al. (2006) and found no counterparts in our data for 50 of their objects. Most of them were detected in only one channel and may therefore be spurious detections such as cosmic ray events. For the objects in common with Young et al. (2006), the differences relative to our photometry are $+0.151 \pm 0.097$ ($N = 50$, 5 excluded),

Table 1
Catalog of Sources Detected with *Spitzer Space Telescope* IRAC and MIPS 24 μm^a

SST	α_{J2000}	δ_{J2000}	[3.6]	[4.5]	[5.8]	[8.0]	[24]	$\epsilon_{[3.6]}$	$\epsilon_{[4.5]}$	$\epsilon_{[5.8]}$	$\epsilon_{[8.0]}$	$\epsilon_{[24]}$	N _{obs}					dup ^a	memb ^b	2MASS	Sung et al. (2008)		
10936	6:40:53.63	9:40:09.2	15.938	15.907	0.064	0.049	4	4	0	0	0						
10937	6:40:53.63	9:29:53.3	13.171	12.908	12.561	11.891	...	0.043	0.058	0.043	0.016	...	7	8	4	4	0		II,H	06405363+0929532		C32434	
10938	6:40:53.63	9:47:04.5	11.887	11.621	11.333	10.857	8.404	0.015	0.040	0.054	0.042	0.300	8	8	7	8	1	D	II,M	06405362+0947043		C32440+C32444	
10939	6:40:53.64	9:33:24.7	10.757	10.558	10.404	10.194	6.880	0.018	0.020	0.021	0.036	0.064	8	8	8	8	1		II/III,+	06405363+0933247		S2564	
10940	6:40:53.64	9:36:46.1	14.787	14.734	14.409	0.016	0.031	0.069	4	4	2	0	0		X	06405362+0936461		C32439	
10941	6:40:53.64	9:34:36.7	15.726	15.311	0.038	0.059	4	4	0	0	0						
10942	6:40:53.64	10:01:08.9	15.094	15.008	0.059	0.096	2	2	0	0	0			06405364+1001087		C32446	
10943	6:40:53.66	9:22:10.0	16.488	16.300	0.086	0.080	4	3	0	0	0						
10944	6:40:53.68	9:23:34.7	15.845	15.792	0.062	0.032	4	4	0	0	0	D					C32445+C32458
10945	6:40:53.67	9:58:00.1	12.730	12.645	12.665	12.655	...	0.032	0.044	0.032	0.095	...	8	8	4	4	0		M	06405367+0958000		C32453	
10946	6:40:53.68	9:31:35.3	16.741	0.006	2	0	0	0	0						
10947	6:40:53.71	9:19:38.3	16.014	16.192	0.027	0.071	4	4	0	0	0						C32463
10948	6:40:53.72	9:18:53.2	17.102	0.087	2	0	0	0	0						C32462
10949	6:40:53.72	9:25:56.5	16.383	0.047	4	0	0	0	0						C32461
10950	6:40:53.73	9:39:16.1	16.435	16.100	0.086	0.040	4	3	0	0	0						
10951	6:40:53.73	9:46:20.8	14.853	14.717	0.025	0.075	4	4	0	0	0						C32468
10952	6:40:53.74	9:46:37.7	...	15.976	0.106	0	3	0	0	0						
10953	6:40:53.76	9:53:46.0	16.053	16.114	0.084	0.016	4	2	0	0	0						C32470
10954	6:40:53.78	9:30:39.0	10.232	10.246	10.202	10.213	...	0.015	0.008	0.009	0.020	...	8	8	8	8	0		X	06405377+0930389		S2568	

Notes. Units of right ascension are hours, minutes, and seconds of time, and units of declination are degrees, arcminutes, and arcseconds.

^a Duplicity—D: SST source having two optical counterparts within 2'' searching radii, T: SST source having three optical counterparts within 2'' searching radii.

^b Membership-IR classification (Class I, II, II/III, pre-TD (pre-transition disk), and TD (transition disk)) and other membership listed in Sung et al. (2008).

(This table is available in its entirety in machine-readable and Virtual Observatory (VO) forms in the online journal. A portion is shown here for guidance regarding its form and content.)

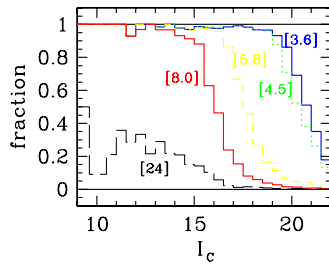


Figure 2. Completeness of *Spitzer* photometry for the 16,772 optical stars in the central region of NGC 2264 covered by all four IRAC channels. The 80% completeness is $I_c = 20, 19.5, 17,$ and 15.5 for [3.6], [4.5], [5.8], and [8.0], respectively. The completeness of [24] is generally below 40%.

(A color version of this figure is available in the online journal.)

$+0.077 \pm 0.127$ ($N = 50, 4$ excluded), $+0.081 \pm 0.137$ ($N = 42, 3$ excluded), and $+0.195 \pm 0.164$ ($N = 32, 2$ excluded) in [3.6], [4.5], [5.8], and [8.0], respectively. The systematic offsets relative to the Young et al. (2006) data may result from their use of aperture photometry (or at least from the fact that we use PSF photometry and they use aperture photometry). We also compared our data with independent aperture photometry determined by I. Song (2008, private communication). The difference in [3.6] is $+0.036 \pm 0.024$ ($N = 51, 7$ excluded). Recently, Cieza & Baliber (2007) published photometric data for 445 stars in NGC 2264. They published data in fluxes rather than in magnitudes. We transformed their data to magnitudes using the photometric zero points in the IRAC Handbook (V3.0). The differences relative to our photometry were $+0.126 \pm 0.052$ ($N = 408, 18$ stars excluded), $+0.158 \pm 0.046$ ($N = 396, 25$ stars excluded), $+0.104 \pm 0.064$ ($N = 312, 40$ stars excluded), and $+0.154 \pm 0.056$ ($N = 184, 18$ stars excluded) in [3.6], [4.5], [5.8], and [8.0], respectively. The differences are relatively large and systematic, but we cannot identify the source of the systematic differences. To help determine the source of the differences, we also calculated and compared the $K_s - [3.6]$ colors for relatively bright, diskless stars in the NGC 2264 field (specifically, stars with $[3.6] - [4.5] < 0.2$ and $[3.6] < 13$). The mean $K_s - [3.6]$ color of our data was $+0.170 \pm 0.104$ ($N = 183$), while that of Cieza & Baliber (2007) was $+0.294 \pm 0.120$ ($N = 183$). As the reddening of stars in NGC 2264 is very small (Sung et al. 1997), the $K_s - [3.6]$ color of Class III objects or photospheres should be close to 0. We believe that the smaller mean $K_s - [3.6]$ color for our photometry supports our contention that our systematic difference relative to Cieza & Baliber (2007) and relative to Young et al. (2006) is due to a zero-point error in their photometry, at least for $3.6 \mu\text{m}$.

2.3. Optical and Two Micron All Sky Survey Counterparts, and X-ray Sources

We searched for optical and 2MASS counterparts to the sources detected in IRAC with a search radius of $1''$. The master optical source catalog we used was created from Tables 3 (“C” + ID objects), 8 (“W” + 4 digit ID objects), and 9 (“S” + ID objects) of Sung et al. (2008). Among 21,991 IRAC objects, 7869 objects have a 2MASS counterpart and 17,932 objects have an optical counterpart. As the optical data had better spatial resolution, five IRAC sources had three optical counterparts and 496 sources had two. Two active PMS stars (C30987 and C30995) were located within the matching circle of SST 10207. The distance between the two stars is about $0''.9$. A strong X-ray emission object (detection significance = 25.59) was also detected at the same position. Dahm & Simon (2005) reported a strong $H\alpha$

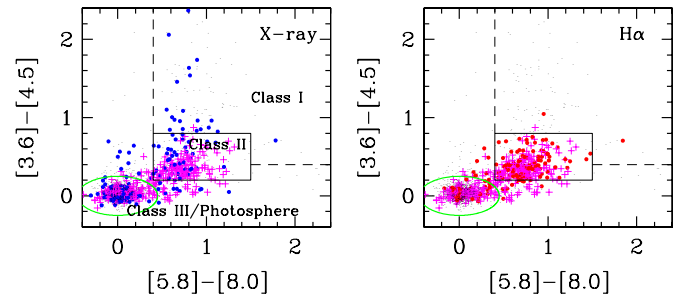


Figure 3. Distribution of X-ray emission stars and $H\alpha$ emission stars in the $([3.6] - [4.5], [5.8] - [8.0])$ diagrams. The large (blue) dots in the left panel represent X-ray emission stars, while a (magenta) plus sign in both panels denotes a star showing emission in both X-ray and $H\alpha$. The large (red) dots in the right panel are $H\alpha$ emission stars. The small dots are stars with no emission in X-ray (left) or in $H\alpha$ (right).

(A color version of this figure is available in the online journal.)

emission source ($W_{H\alpha} = 458.2 \text{ \AA}$). Either or both stars could be the optical counterpart of SST 10207. As in most cases Class I objects do not have normal optical colors, we tentatively identify the faint BMS star C30995 as the optical counterpart of the Class I star SST 10207. The one Class I star that we believe does fall in the PMS locus is SST 12918 (=C35527), an X-ray emission star.

To check for completeness relative to the optical photometry, we identified *Spitzer* counterparts of optical sources in the central region of NGC 2264 covered by all four IRAC channels. The area is 1204 arcmin^2 . There were 16,772 optical stars, excluding stars where a single *Spitzer* source is matched to two or more optical stars (522 optical stars in total). The completeness is shown in Figure 2. The 80% completeness level was $I_c = 20, 19.5, 17,$ and 15.5 for [3.6], [4.5], [5.8], and [8.0], respectively. Fainter than that, the detection fraction decreases rapidly. Because stellar photospheres are relatively faint at $24 \mu\text{m}$, the detection fraction in [24] is generally less than 40%.

In addition, we also searched for any new IR counterparts of X-ray sources (X-ray sources from Sung et al. 2004, 2008; from Ramírez et al. 2004; and from Flaccomio et al. 2006 were included). We identified 52 IRAC sources as new counterparts of X-ray sources with significance > 5 and 30 IRAC sources as counterparts of weak X-ray sources with significance between 3.3 and 5.0. Among them, SST 13029, rather than C35645 in Table 3 of Sung et al. (2008), is the actual counterpart of X-ray source F06–264 (Flaccomio et al. 2006; CXO J0641071+0930366). Many of the new X-ray counterparts are embedded Class I or II objects. Some of them may be unseen active galaxies. We list *Spitzer* data for the 43 X-ray sources without previous optical or 2MASS counterparts in Table 2.

The optical and 2MASS data for all *Spitzer* sources are listed in Table 1. In addition, other information related to cluster membership such as $H\alpha$ emission or X-ray emission (both for our new IR counterparts and for objects previously cross-identified with X-ray sources based on optical and near-IR data) is also included. Figure 3 shows the distribution of all NGC 2264 X-ray emission and $H\alpha$ emission sources in the $([3.6] - [4.5], [5.8] - [8.0])$ diagram. We adopt the classification scheme of Megeath et al. (2004) and Allen et al. (2004, 2007b). Large dots represent either X-ray emission stars (left) or $H\alpha$ emission stars (right), while plus marks denote stars with emission in both X-ray and $H\alpha$. Most of the $H\alpha$ emission stars are distributed in the region occupied by Class II and Class III/Photosphere stars. Only three $H\alpha$ stars are in the locus of Class I objects. On the other hand,

Table 2
Spitzer Counterparts of X-ray Sources without Optical or 2MASS Counterparts

SST	α_{J2000}	δ_{J2000}	[3.6]	[4.5]	[5.8]	[8.0]	[24]	$\epsilon_{[3.6]}$	$\epsilon_{[4.5]}$	$\epsilon_{[5.8]}$	$\epsilon_{[8.0]}$	$\epsilon_{[24]}$	N _{obs}	Class	Signif ^a	dist(")
5721	6:40:20.12	9:45:10.9	14.762	14.054	13.672	11.892	8.523	0.029	0.029	0.080	0.060	0.262	4 4 4 4 1	Galaxy	25.4	0.3
6944	6:40:27.73	9:41:19.8	16.595	15.875	0.075	0.025	2 4 0 0 0		7.8	0.9
7546	6:40:31.61	9:44:26.8	15.537	15.115	0.037	0.047	4 4 0 0 0		8.8	0.4
8077	6:40:34.90	9:44:23.2	16.174	15.727	0.525	0.036	1 4 0 0 0		5.2	0.8
8097	6:40:35.04	9:39:54.4	15.567	15.412	0.040	0.056	4 4 0 0 0		7.0	0.7
8221	6:40:35.81	9:52:00.5	14.768	14.733	0.038	0.020	2 2 0 0 0		6.3	1.0
8614	6:40:38.16	9:32:01.4	16.110	14.734	0.056	0.642	4 4 0 0 0		4.9	0.3
8715	6:40:38.77	9:51:44.8	15.351	15.205	0.051	0.019	4 4 0 0 0		4.2	1.1
9444	6:40:43.62	9:31:14.9	16.028	15.623	0.079	0.053	4 4 0 0 0		4.3	1.3
9735	6:40:45.49	9:37:06.7	16.572	16.167	0.009	0.050	4 2 0 0 0		4.2	0.8
9934	6:40:46.83	9:32:16.8	...	15.763	0.110	0 4 0 0 0		4.4	0.4
10274	6:40:49.09	9:31:56.5	16.290	16.238	0.023	0.441	3 1 0 0 0		3.8	0.5
10453	6:40:50.28	9:33:11.3	15.310	15.049	0.023	0.051	4 4 0 0 0		4.1	0.8
10493	6:40:50.47	9:32:19.6	...	16.150	0.087	0 3 0 0 0		20.8	0.5
10858	6:40:52.97	9:32:43.2	16.134	15.710	0.061	0.061	4 4 0 0 0		4.3	0.8
11102	6:40:54.67	9:53:04.4	16.310	15.529	0.018	0.055	2 4 0 0 0		4.7	0.6
11257	6:40:55.77	9:54:11.5	...	15.928	0.015	0 2 0 0 0		3.5	0.6
11315	6:40:56.17	9:37:55.1	15.936	15.584	0.065	0.034	4 4 0 0 0		4.0	1.3
11592	6:40:57.98	9:36:39.5	11.279	9.541	8.540	7.645	4.040	0.064	0.062	0.051	0.039	0.013	8 8 8 8 1	I	5.4	0.4
11598	6:40:58.01	9:36:14.6	12.892	11.805	11.077	10.341	6.682	0.028	0.038	0.031	0.014	0.066	8 8 8 8 1	I	4.1	0.3
11711	6:40:58.68	9:52:53.6	13.978	13.928	13.695	12.441	...	0.031	0.044	0.067	0.334	...	5 4 3 1 0		7.3	0.0
11713	6:40:58.70	9:54:16.1	13.286	13.160	12.925	0.041	0.105	0.058	8 6 4 0 0		9.6	0.4
12412	6:41:03.21	9:44:44.2	16.208	15.272	0.044	0.068	4 4 0 0 0		5.3	1.0
12637	6:41:04.61	9:36:18.3	10.832	9.374	8.619	7.950	...	0.035	0.028	0.012	0.023	...	8 8 8 8 0	I	40.1	0.4
12681	6:41:05.01	9:41:04.7	16.289	16.078	0.043	0.074	4 4 0 0 0		4.0	0.5
12722	6:41:05.23	9:36:31.9	12.252	11.522	10.110	0.098	0.104	0.119	1 8 8 0 0		5.8	0.5
12774	6:41:05.53	9:35:01.4	14.083	13.732	13.221	12.694	...	0.033	0.059	0.069	0.014	...	4 4 4 2 0	II	4.1	0.2
12780	6:41:05.56	9:34:08.0	12.312	10.675	9.612	8.809	3.544	0.033	0.047	0.038	0.012	0.100	4 3 8 8 1	I	5.9	0.9
12831	6:41:05.87	9:34:46.0	11.427	11.281	10.855	10.996	...	0.026	0.014	0.078	0.097	...	8 8 8 8 0	II/III	65.4	0.4
12875	6:41:06.19	9:34:08.8	12.664	10.604	9.831	9.255	3.576	0.060	0.030	0.021	0.019	0.072	8 8 8 8 1	I	3.7	0.6
13029	6:41:07.16	9:30:36.3	11.195	10.637	10.097	9.457	6.003	0.060	0.036	0.043	0.017	0.100	8 8 8 8 1	II	13.3	1.0
13085	6:41:07.47	9:36:10.8	14.458	13.612	13.114	0.049	0.028	0.086	4 4 4 0 0		3.9	1.1
13111	6:41:07.67	9:34:19.1	13.621	11.252	9.980	9.185	4.095	0.070	0.022	0.020	0.013	0.019	8 8 8 8 1	I	34.4	0.5
13672	6:41:11.61	9:29:10.3	13.291	11.254	10.135	0.113	0.063	0.072	6 8 7 0 0		5.6	0.6
13749	6:41:12.22	9:29:14.5	12.249	10.869	0.188	0.170	7 8 0 0 0		6.7	0.3
14094	6:41:14.49	9:35:37.5	15.894	14.534	0.047	0.055	3 3 0 0 0		3.6	0.9
14144	6:41:14.84	9:29:17.3	15.650	14.758	0.070	0.355	4 1 0 0 0		3.7	0.7
14338	6:41:16.41	9:52:49.7	16.582	15.482	0.095	0.044	4 4 0 0 0		10.2	0.8
14371	6:41:16.65	9:52:06.8	...	16.535	0.067	0 2 0 0 0		6.9	0.4
14834	6:41:19.72	9:31:39.0	15.198	15.063	0.052	0.038	4 4 0 0 0		6.2	1.0
15746	6:41:25.79	9:40:35.5	16.651	16.065	0.055	0.188	4 3 0 0 0		7.0	1.0
16270	6:41:29.08	9:39:49.4	16.156	15.479	0.023	0.041	4 4 0 0 0		11.9	1.0
16562	6:41:31.03	9:35:25.4	16.335	15.506	0.036	0.039	4 4 0 0 0		9.9	0.5

Note.

^a X-ray detection significance from “pwdetect” (see Sung et al. 2004; Flaccomio et al. 2006).

X-ray emission objects are more widely distributed. There are many X-ray sources in the region occupied by Class I or highly reddened objects. These very red ($[3.6] - [4.5] > 1.5$) X-ray emission objects are located in the Spokes cluster or the Cone nebula region, and therefore are almost certainly deeply embedded Class I objects rather than background active galaxies.

2.4. Very Red Objects

2.4.1. Objects that are Red in $[5.8] - [8.0]$

There are a total of 38 objects with $[5.8] - [8.0] > 1.5$ mag. We carefully examined the long exposure optical images obtained with the Canada–France–Hawaii Telescope (CFHT) (see Sung et al. 2008) to help determine their nature. Based on our examination of the optical images, we classify 22 of these objects as galaxies—three are obvious galaxies and 19 appear as diffuse objects, which we believe are best interpreted as galaxies.

These 22 objects are marked as “Galaxy” in the 20th column of Table 1. Three objects are point sources that have been identified as having $H\alpha$ emission. Two of them are BMS stars with $H\alpha$ emission—the well-known BMS stars W90 (=S2144 = SST 9597) and C31519 (= SST 10475). One is a suspected BMS star (C32005 = SST 10710 = Ogura 97)—Ogura (1984) classified the star as an $H\alpha$ emission star, but the star showed no indication of $H\alpha$ emission from our $H\alpha$ photometry. Two other optical counterparts are point sources in the optical without detected $H\alpha$ emission—both lie below the PMS locus in the I_C versus $(R-I)_C^0$ CMD. We could find no optical counterparts for the remaining 11 objects.

2.4.2. Objects that are Red in $[3.6] - [4.5]$

We also examined the optical images of 25 objects that were very red in $[3.6] - [4.5]$ ($[3.6] - [4.5] > 0.4$ mag and $[5.8] - [8.0] < 0.4$ mag). This region in the IRAC C–C plane is known

as the locus of reddened Class II objects (Allen et al. 2004). We could find no optical counterparts for 20 of the objects. Most of them are in regions of bright nebosity. This fact supports the proposition that objects in this region of the C–C diagram is probably embedded and therefore highly reddened. Five objects are detected in the optical and are point sources. One of them is probably a field star, where the red [3.6] – [4.5] color is probably not real but due to a large error in the photometry. The other four stars have H α emission and are probably YSOs (one is an X-ray emission star and another is a BMS star).

2.5. Galaxy Contamination

As mid-IR photons are less affected by interstellar reddening, contamination of cluster stars by external galaxies is inevitable. The galaxies with red [5.8] – [8.0] colors mentioned in Section 2.4.1 are bright in [8.0] due to 7.7–8.2 μm polycyclic aromatic hydrocarbon (PAH) emission excited by young, high-mass stars (Stern et al. 2005; Gutermuth et al. 2008). But as mentioned above, a well-known Herbig Be star W90 (= S2144) also shows emission in [8.0] (see also Keller et al. 2008). Star S2975 (= SST 12833) and SST 10184 (= C30920+C30962) show similar characteristics (H α emission and [8.0] emission).

We constructed SEDs for all of our candidate PMS objects and identified all objects where the [8.0] flux is significantly brighter than a curve drawn through the other IRAC fluxes (extending to the 24 μm point where the object is detected at 24 μm). For the objects with significant flux excess at 8 μm , we examined our deep optical images at the coordinate of these objects. Among eight objects with PAH emission (excluding the objects already mentioned in Section 2.4.1 and the above paragraph), we recently identified SST 6182 and 19807 as galaxies, but no optical counterparts could be found for SST 10914, 11099, 13654, 14676, 14997, and 17616.

Gutermuth et al. (2008) found the locus of star-forming galaxies (SFGs) dominated by PAH emission in the ([3.6] – [5.8], [4.5] – [8.0]) and ([4.5] – [5.8], [5.8] – [8.0]) diagrams. There are 22 objects in our NGC 2264 data that fall within the Gutermuth et al. (2008) SFG locus in the ([4.5] – [5.8], [5.8] – [8.0]) diagram. Thirteen of these objects have 8 μm excesses according to our SED analysis and were classified as galaxies based on our examination of the deep CFHT images. Two more of the objects in the SFG locus were also classified by us as galaxies but do not show 8 μm excesses. The remaining seven objects in the SFG locus are SST 10184, 10914, 11099, 13654, 14676, 14997, and 17616, respectively. SST 10184 has two optical counterparts (C30920 and C30962) within the search radius. If the actual counterpart is C30962, then SST 10184 could be a faint SFG. As SST 10914 (Class II) and SST 11099 (Class I) are in the two active SFRs (Spokes and Cone (C)—see Section 4.1), they could be deeply embedded YSOs. Three objects (SST 14676, 14997, 17616) without optical counterparts are in the Halo or Cone (H) regions, and therefore they may be SFGs with PAH emission. The other two objects have spatial locations that do not allow us to confidently identify them as galaxies or YSOs.

The results from the ([3.6] – [5.8], [4.5] – [8.0]) diagram are nearly the same as above. Only one object identified in the ([4.5] – [5.8], [5.8] – [8.0]) diagram as a PAH emission SFG, SST 5721 (an optically confirmed galaxy), was missed in the ([3.6] – [5.8], [4.5] – [8.0]) diagram.

In addition to SFGs with [8.0] PAH emission, AGNs also show excess emission in the IR. The locus of AGNs overlaps with that of Class I objects in IR C–C diagrams. Gutermuth

et al. (2008) filtered out broad-line AGN candidates using color and magnitude cuts in the [4.5] versus [4.5] – [8.0] diagram (including eliminating all objects fainter than [4.5] > 14.5). We have attempted a different approach, by directly examining deep optical images of all 95 Class I objects selected in Section 3.1. Among them, 68 objects had no optical counterpart (nothing seen). Most of them were clustered around the Spokes cluster or the Cone nebula; we believe that their spatial location makes it highly likely that these objects are deeply embedded YSOs. Ten objects were point sources in the deep optical images. Among the 10 point sources, five objects (SST 2558, 10207, 11837, 12918, and 13288) were surrounded by a thin nebosity (i.e., the wings of the PSF are slightly elevated). SST 2558 is an H α emission star (# 45 of Reipurth et al. 2004), and may be an optical counterpart of *ROSAT* X-ray emission object 1WGA J0640.1+0943. Because of these properties, and because it is relatively bright ($I_C = 17.8$ mag), we believe that it is unlikely that SST 2558 is an external galaxy. The other four objects are located either in the Spokes cluster or in the Cone nebula, and therefore we assume that they are exposed YSOs with nebula around them. Another eight objects were very faint, and it was difficult to discern whether they were faint stars or galaxies. We found extended nebosity at the coordinates of five objects (SST 12208, 12253, 12583(?), 13566, and 14214), but the nebulae seem to be excited by embedded YSOs (i.e., the nebulae were structured or asymmetric, unlike what we would expect for a distant galaxy). Four of the sources (SST 4787, 6262, 16492, and 21671) were diffuse, and based on our experience they are most likely galaxies (they are marked as “Galaxy” in the 20th column of Table 1). Because we found several galaxies close in vicinity to SST 8501, 9861, and 21808, we suspect that these sources are galaxies and members of small groups or clusters. In total, seven of the Class I objects are best categorized as galaxies based on our examination of the deep optical images, 21 of the Class I objects cannot be verified or rejected, and 67 of the Class I objects are best interpreted as YSOs (because of their spatial location or association with asymmetric nebulae). In support of our analysis, we note that the visually identified or suspected galaxies are more or less randomly scattered throughout the outer portion of the IRAC field of view (see Figure 13).

2.6. Variability

One of the important characteristics of YSOs is their photometric variability. Several attempts have been made to detect variability in the *Spitzer* data. Rebull et al. (2007) and Harvey et al. (2007) searched for variability of YSOs in Serpens or Perseus, but due to the short time span they could not detect variability above the 10% or 20% level. Recently, Vijn et al. (2008) detected the variability of objects in the Large Magellanic Cloud from the SAGE (Surveying the Agents of a Galaxy’s Evolution) survey. In addition, Morales-Calderon et al. (2008) obtained the most extensive IRAC monitoring of a YSO field to date, consisting of twice daily monitoring of the IC 1396A star-forming core. They found that > 1/3 of the YSOs in this ~ 1 Myr cluster are variable at IRAC wavelengths, with amplitudes of up to 0.2 mag; about a dozen of the sources appeared to be periodic variables, most with periods of the order of 3–10 days, but with one star having a 3.5 hr period (a possible PMS δ Scuti star).

Because we have four sets of data observed at two widely separated epochs, it is worthwhile to check for variability in our catalog. Vijn et al. (2008) introduced a variability index based upon the error-weighted flux difference between two epochs

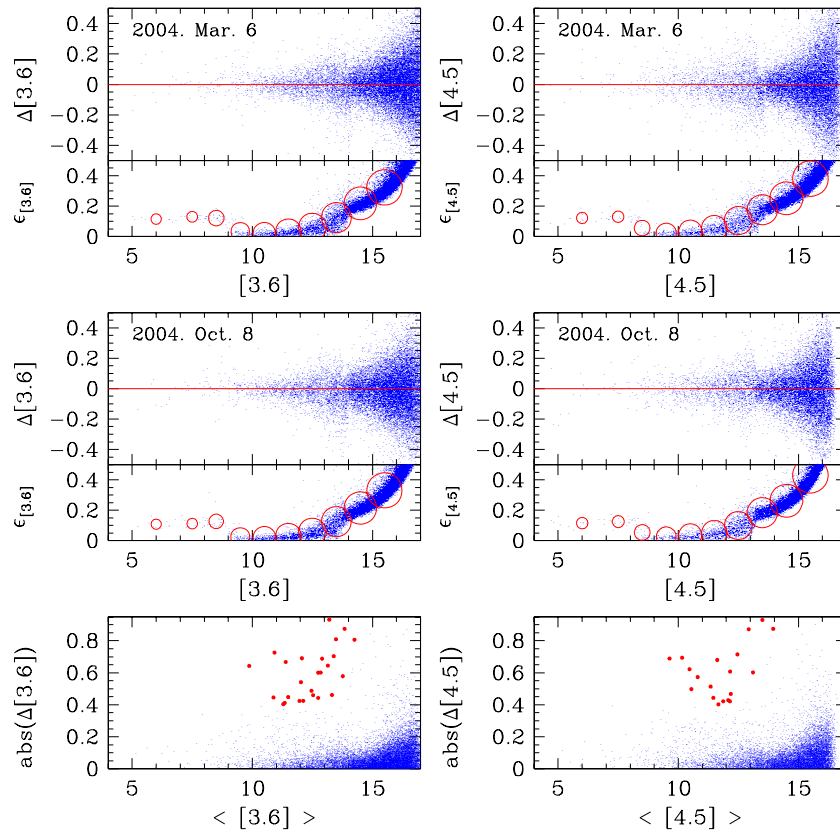


Figure 4. Variability test at $3.6 \mu\text{m}$ (left panels) and $4.5 \mu\text{m}$ (right panels). The upper two panels show the magnitude difference and total error of data obtained on 2004 March 6. The open circles in the second panel represent the mean errors for a given magnitude bin. The size is proportional to the number of stars in the bin. The middle two panels show similar plots for 2004 October 8. The lowest panels show the distribution of magnitude differences between the two epochs. The large red dots denote variable candidates.

(A color version of this figure is available in the online journal.)

in order to search for variables. We have searched for variable objects in NGC 2264 in a similar way. First, we calculated the weighted mean and total error (square root of the quadratic sum of photometric errors for each set) in [3.6] and [4.5] for data obtained on the same date. We then calculated the differences in magnitude, the ratio of the difference, and the total error for a given passband. If the difference between two epochs was greater than 3.5 times the total error and greater than about 0.4 mag—the photometric error of DAOPHOT undersampled data was about 0.1 mag—then we classified the object as a variable source. In this process, we selected 28 variable candidates. Figure 4 shows the distribution of brightness difference between two data sets obtained on the same date (uppermost and middle panel) as well as between two widely separated epochs in the lowest panel. The left panel is for [3.6] and the right panel is for [4.5]. The large dots in the lowest panels represent the variable candidates selected from this work and listed in Table 3. The number of sources showing variability is actually a lower limit because we performed PSF photometry which gives a larger photometric error for the undersampled data. A reanalysis of the data using aperture photometry would undoubtedly identify a larger number of stars that are variable at IRAC wavelengths.

In total, 28 variable candidates were selected. In general, the variation pattern and amplitude in [3.6] and [4.5] were very similar. Only two objects (SST 13432 and 13612) showed a variation > 0.4 mag in one channel but only a small (< 0.15 mag) delta magnitude in the other channel—the variations in these two stars may be spurious. Among the 28 variable candidates,

four objects were classified as Class I, eight were Class II, and three were intermediate between Classes II and III (see Section 3 for the classification scheme). The other candidates were not classified because of a lack of either [5.8] or [8.0] data or large errors at the long wavelengths. But most of the remaining variable candidates are very red. Based on a review of the photometry, we can offer tentative classifications for five of the remaining stars. Although the photometric errors are large, SST 11699 and 14514 should probably be classified as Class I. SST 15726 is probably of Class II and SST 13123 is on the border between Classes I and II. SST 8570 was detected in all IRAC channels with somewhat larger errors and is a Class III or normal star. The others were only detected in [3.6] and [4.5] and their [3.6] – [4.5] colors are red.

3. CLASSIFICATION OF YOUNG STARS

Lada & Wilking (1984) presented the SEDs of deeply embedded YSOs in ρ Oph. Later, Lada (1987) introduced the slope of the SED, $\alpha \equiv \frac{d \log(\lambda F_\lambda)}{d \log \lambda}$, to classify YSOs. Now, the slope of the SED is a basic tool with which to diagnose the evolutionary stage of YSOs. The innovative development of two-dimensional photodetectors in the IR, such as IRAC and MIPS on the *Spitzer Space Telescope*, makes it possible to observe many YSOs in a single image; as a result, the number of YSOs from a single observation can increase from a few up to several hundreds. This large increase in the number of objects considered has made photometric methods based on photometric C–C diagrams a much more powerful way to

Table 3
Variables Detected in IRAC [3.6] and [4.5]

SST	[3.6] _{2004.Mar.6}	[3.6] _{2004.Oct.8}	Δ [3.6]	[4.5] _{2004.Mar.6}	[4.5] _{2004.Oct.8}	Δ [4.5]	Class	other	Sung et al. (2008)
6655	11.054 ± 0.003	11.721 ± 0.034	-0.667	10.520 ± 0.008	11.093 ± 0.005	-0.574	II	H α	C23131
7009	14.055 ± 0.025	13.477 ± 0.157	+0.578	13.705 ± 0.024	13.436 ± 0.012	+0.269	II/III		C23941
7252	12.823 ± 0.006	13.468 ± 0.026	-0.644	11.853 ± 0.037	12.461 ± 0.013	-0.608	I		
7899	12.149 ± 0.006	11.795 ± 0.001	+0.354	12.082 ± 0.073	11.660 ± 0.007	+0.422	II/III	X+H α	C26021
8570	13.546 ± 0.093	13.085 ± 0.025	+0.461	13.523 ± 0.018	13.246 ± 0.027	+0.277			C27455
9117	9.924 ± 0.054	9.548 ± 0.010	+0.376	9.544 ± 0.003	9.179 ± 0.010	+0.365	II	X+H α	S1968
9322	11.492 ± 0.005	11.089 ± 0.009	+0.403	11.122 ± 0.000	10.867 ± 0.036	+0.255	II/III	X+H α	C29082
10455	12.518 ± 0.028	12.961 ± 0.004	-0.443	10.507 ± 0.012	10.890 ± 0.033	-0.382	I		
11699	13.886 ± 0.022	13.076 ± 0.049	+0.810	12.818 ± 0.019	12.103 ± 0.007	+0.715		X	
11802	12.295 ± 0.002	11.754 ± 0.001	+0.541	10.794 ± 0.009	10.298 ± 0.020	+0.496	I		
11903	12.947 ± 0.009	12.632 ± 0.003	+0.315	12.360 ± 0.020	11.939 ± 0.020	+0.421	II		
12051	12.329 ± 0.033	11.904 ± 0.019	+0.425	11.874 ± 0.031	11.470 ± 0.032	+0.404	II	X+H α	C34222
12722	12.252 ± 0.098	10.997 ± 0.031	11.682 ± 0.002	-0.685		X	
13123	12.441 ± 0.003	12.990 ± 0.106	-0.549	11.359 ± 0.013	12.991 ± 0.088	-1.632			
13241	12.409 ± 0.004	11.719 ± 0.028	+0.690	...	11.287 ± 0.044	...			
13259	13.247 ± 0.020	12.558 ± 0.001	+0.688	11.733 ± 0.018	11.354 ± 0.003	+0.379			
13295	11.443 ± 0.009	12.524 ± 0.056	-1.080			C36017
13306	10.561 ± 0.003	11.287 ± 0.026	-0.726	9.291 ± 0.019	9.981 ± 0.039	-0.690	I		
13401	14.277 ± 0.001	13.403 ± 0.049	+0.874	13.366 ± 0.012	12.494 ± 0.019	+0.872			
13432	12.857 ± 0.048	12.972 ± 0.118	-0.115	12.059 ± 0.054	13.051 ± 0.016	-0.992		X+H α	C36216
13480	10.659 ± 0.027	11.105 ± 0.060	-0.445	9.813 ± 0.003	10.508 ± 0.002	-0.695	II	X	
13612	12.581 ± 0.001	12.475 ± 0.027	+0.106	12.295 ± 0.010	11.867 ± 0.009	+0.429	II		
13715	12.217 ± 0.014	12.704 ± 0.062	-0.488		H α	C36610
13734	11.143 ± 0.028	11.555 ± 0.027	-0.412	10.571 ± 0.030	10.886 ± 0.015	-0.315	II	X+H α	C36644
13749 ^a	13.144 ± 0.058	12.543 ± 0.043	+0.601	11.603 ± 0.095	11.090 ± 0.031	+0.513		X	
14514	14.474 ± 0.036	13.851 ± 0.043	+0.623	13.411 ± 0.021	12.810 ± 0.127	+0.602			
15726	12.173 ± 0.006	11.750 ± 0.019	+0.423	11.964 ± 0.041	11.283 ± 0.000	+0.681		X+H α	C39809+C39817
16833	12.796 ± 0.018	12.512 ± 0.003	+0.284	12.419 ± 0.001	11.951 ± 0.009	+0.468	II	H α	C41880

Note.

^a Used only data from long exposure images because short and long exposure images show large systematic differences probably due to the nearby bright star SST 13808.

classify the evolutionary stage of YSOs. In addition, modeling techniques have also improved (Allen et al. 2004; Robitaille et al. 2007), resulting in better predictions of the locus of YSOs at a given evolutionary stage.

In this section, we attempt to classify the stars detected from the *Spitzer* images of NGC 2264 using primarily photometric colors. We also use the SED method as an ancillary tool.

3.1. *Spitzer* Color–Color Diagrams

Megeath et al. (2004) introduced the classification criteria in the ([3.6] – [4.5], [5.8] – [8.0]) C–C diagram. Later, slight modifications (Harvey et al. 2007; Gutermuth et al. 2008) or the inclusion of MIPS [24] data (Allen et al. 2007b) were made. In the classification of YSOs in NGC 2264, we basically used the locus of YSOs introduced by Megeath et al. (2004) and Allen et al. (2007b) and extended them to other C–C diagrams. The locus of Class III and stellar-photosphere stars was assumed to be an ellipse around (0, 0) in the C–C diagram. In addition, we adopted a weighting scheme in the classification because in many cases the class of a YSO from one C–C diagram differs with that from other C–C diagrams. Two kinds of weights were used—the first ($q_i = 1.5, 0.7, 1.0,$ and 1.5×1.5 for C–C diagrams in Figure 5 from the upper left, upper right, lower left, and lower right, respectively) was related to the classification resolution (e.g., the class of a YSO from the ([3.6] – [4.5], [5.8] – [8.0]) diagram was more reliable than that from the ([3.6] – [4.5], [4.5] – [5.8]) diagram) and the second (w_i) was related to the data quality (i.e., photometric errors). We assigned $w_i = 0.3, 0.7,$ and 1.5 for bad, fair, and good data, respectively (“bad”

if the individual error of all relevant colors was greater than 0.1 mag, “good” if the individual error of all relevant colors was smaller than 0.1 mag and the total error was smaller than 0.2 mag, and “fair” if the error was between them). As the main purpose of this study was to select members of the young open cluster NGC 2264, we assume that objects outside the locus of Class I or Class III/Photosphere are of Class II. Then, the mean value of a YSO class (Cl_i) (call this quantity Q_{CC}) is

$$Q_{CC} \equiv \frac{\sum_i Cl_i \cdot q_i \cdot w_i}{\sum_i q_i \cdot w_i}.$$

If Q_{CC} is equal to or less than 1.5, the object is assigned to Class I. If Q_{CC} is smaller than 2.3, the object is assigned to Class II. And if Q_{CC} is between 2.3 and 2.7, the object is of Class II/III (an object intermediate between Classes II and III). Practically, we only classified objects detected in all four IRAC colors with good quality data (a quadratic summed total error in all four IRAC channels of less than 0.25 mag).

3.2. Spectral Energy Distribution

The slope of the SED from IRAC [3.6] to MIPS [24] was calculated for the objects detected in all four IRAC channels. In the calculation of the SED slope, we used a weighted linear fit to the derived fluxes. The weight applied was the inverse of the quadratic sum of the photometric errors and the uncertainty in the photometric zero point (assumed to be 0.05 mag). The adopted flux of the 0th magnitude stars and the effective wavelengths from the optical to near-IR are those by Bessell et al. (1998). For *Spitzer* passbands, these values were

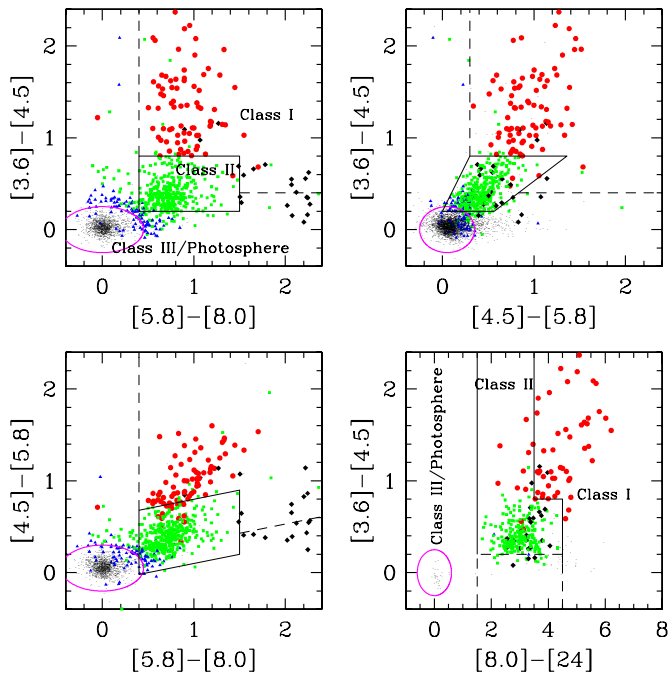


Figure 5. Distribution of YSOs in various C–C diagrams. The loci of Class I and II objects are adopted from Megeath et al. (2004) and Allen et al. (2007b), respectively. A large red dot, green square, and blue triangle denotes, respectively, Class I, II, and II/III (intermediate between Class II and III) objects based on the weighting scheme described in the text, respectively. Black diamonds represent optically confirmed background galaxies. Small dots are either Class III objects, stellar photospheres, or objects having bad quality data. We assume that the locus of Class III/Photosphere objects is an ellipse.

(A color version of this figure is available in the online journal.)

taken from the IRAC and MIPS Data Handbooks⁷ (versions 3.0 and 3.3.0, respectively).

To calculate the reddening-corrected SEDs, a reddening law should also be adopted. In general, that for the *UBV* passbands is well known and agrees for different objects (see Bessell et al. 1998; Fitzpatrick 1999), but those for R_C to the mid-IR differ markedly (see Indebetouw et al. 2005; Chapman et al. 2008). For consistency, we adopted the reddening law from Bessell et al. (1998) for the optical to the near-IR, but for *Spitzer* passbands we derived color excess ratios from the slope of reddened stars in Figure 10. The color excess ratios ($E(K_s - [\text{IRAC}])/E(J - H)$) derived from Figure 10 are 0.39, 0.47, 0.56, and 0.555 for [3.6], [4.5], [5.8], and [8.0], respectively. It is not easy to compare the ratios because $A_{[\text{IRAC}]} / A_{K_s}$ are also affected by the adopted color excess ratios. If we adopt $A_{J,H,K_s} / A_{K_s}$ of Indebetouw et al. (2005), our IR reddening law is similar to dust models of Weingartner & Draine (2001) with $R_V = 3.1$. If we adopt the color excess ratios of Bessell et al. (1998), then A_λ / A_{K_s} of our IR reddening law is similar to that derived for the case of $A_{K_s} \geq 2$ of Chapman et al. (2008). Currently, we use the former case as we have adopted the color excess ratios of Bessell et al. (1998). The color excess ratio for [24] shows a large variation (see Table 3 of Chapman et al. 2008). We tentatively assume that $A_{[24]} / A_{K_s}$ is the same as $A_{[8.0]} / A_{K_s}$.

In the classification of the evolutionary stage of YSOs using the slope of the SED, we adopted the classification scheme of Greene et al. (1994) and Lada et al. (2006). Lada et al. (2006)

defined objects with primordial disks as those with $\alpha > -1.8$ rather than using the classical Greene et al. (1994) definition of Class II objects ($\alpha > -1.6$). Dahm & Hillenbrand (2007) calculated the fraction of stars with primordial disks using the same Lada et al. criterion and as we would also like to calculate the disk fraction and compare it with previous work, we will use the same criterion ($\alpha \geq -1.8$) for Class II.

Class I: $\alpha \geq +0.3$

Flat: $+0.3 > \alpha \geq -0.3$

Class II: $-0.3 > \alpha \geq -1.8$

Class III: $-1.8 > \alpha \geq -2.55$.

We present several typical SEDs in Figure 6. The first sample is the SED for S Mon (O7V), the most massive star in NGC 2264. Ideally the slope of the SED of early-type stars should be -3.0 , but due to the uncertainty in the calibration of the 0th magnitude in the mid-IR, the derived slope is $-2.94 (\pm 0.03)$. The synthetic spectra superposed are Castelli’s Kurucz model atmosphere (see Bessell et al. 1998). The second SED is that of the well-known BMS Herbig Be star W90. More discussion on W90 is presented in Section 7.2.1. The third example is the SED of a Class I object in the PMS locus—C35527 (see Section 7.2.2 for more details). The model atmosphere superposed is the NextGen model atmosphere (Hauschildt et al. 1999) for PMS stars (<ftp://ftp.hs.uni-hamburg.de/pub/outgoing/phoenix/Pre-MS>). The spectral resolution of the theoretical fluxes were reduced for purposes of presentation. The 2MASS colors of C35527 do not show any signature of excess emission when we fit the photometry up to K_s . Close examination of this fit suggests that a cooler model photosphere (than the $T_{\text{eff}} = 2600$ K model we derived) might be more appropriate, but the NextGen models for PMS stars only provide spectra for temperatures between 2600 and 6800 K. As a result, the reddening may be overestimated. The next two SEDs are that of the FU Ori candidate AR 6A and its companion candidate AR 6B (Aspin & Reipurth 2003; see Section 7.2.3). The last SED is the SED for a SFG (see Section 2.4.1). The galaxy was measured as three point sources, but the I_C -band image shows that they are three bright regions in a galaxy. The $8 \mu\text{m}$ PAH feature is prominent in the SFGs. A more detailed analysis of YSO SEDs in NGC 2264 will be presented in A. Bayo et al. (2009, in preparation).

We also classified objects with pre-transition disks (Espaillat et al. 2008) or transition disks. See Evans et al. (2009) for physical and observational definitions of these terms. Cieza et al. (2007) introduced two parameters (λ_{TO} and α_{ex}) to characterize the transition disks. λ_{TO} is the wavelength at which the IR excess begins and α_{ex} represents the SED slope at wavelengths longer than λ_{TO} . They showed a diversity in α_{ex} of WTTs and interpreted it as a wide range of inner disk radii and temperatures compared to classical T Tauri stars (CTTs). We have also found several stars in NGC 2264 whose SED indicated the existence of transition disks. Some stars showed a change in the SED slope at [5.8], but many showed the change at [8.0]. In general, the difference in λF_λ between [5.8] and [8.0] was not very large. For simplicity and to avoid ambiguity due to errors in the SED slope, we have assumed that λ_{TO} occurred at [8.0]. If λF_λ at [8.0] were smaller than the quantity at [24] and the sign of the SED slope α from the IRAC bands (α_{IRAC}) and that between [8.0] and [24] (α_{LW}) differed, then we classified the object as a Class II object with a pre-transition disk if $\alpha_{\text{IRAC}} = -0.3$ to -1.8 or as an object with a transition disk if $\alpha_{\text{IRAC}} < -1.8$. In some cases, λ_{TO} occurred at [5.8]; for these we calculated and used α_{IRAC} between [3.6] and [5.8] rather than α_{IRAC} for all IRAC bands. The distribution of objects with pre-transition or transition disks

⁷ $F_{\nu,0}$ of the 0th magnitude star is 280.9 ± 4.1 Jy, 179.7 ± 2.6 Jy, 115.0 ± 1.7 Jy, 64.1 ± 0.9 Jy, and 7.14 ± 0.0815 Jy for IRAC $3.6 \mu\text{m}$, $4.5 \mu\text{m}$, $5.8 \mu\text{m}$, $8.0 \mu\text{m}$, and MIPS $24 \mu\text{m}$, respectively.

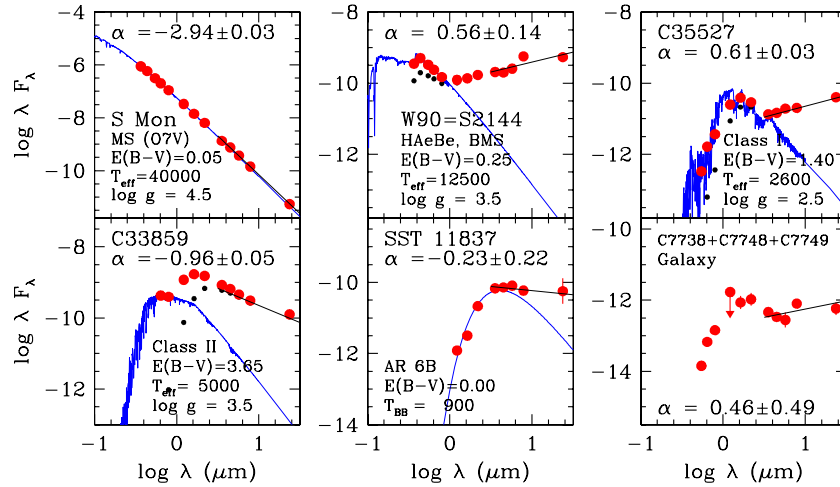


Figure 6. Typical SEDs. The SEDs presented here are the SED of S Mon (O7V, typical stellar photosphere): the flux of a Castelli-Kurucz model atmosphere (see Bessell et al. 1998; upper left); of a below the main-sequence Herbig Be star W90 (= S2144): Castelli-Kurucz flux (upper middle); of a Class I object in the PMS locus: PMS model atmosphere from NextGen (upper right); of a FU Ori type candidate AR 6A and its companion AR 6B (lower left and lower middle); and of a SFG (lower right). Optical photometric data are from Sung et al. (2008) and near-IR data are from 2MASS (Skrutskie et al. 2006) except for AR 6B. The near-IR data for AR 6B are from Aspin & Reipurth (2003).

(A color version of this figure is available in the online journal.)

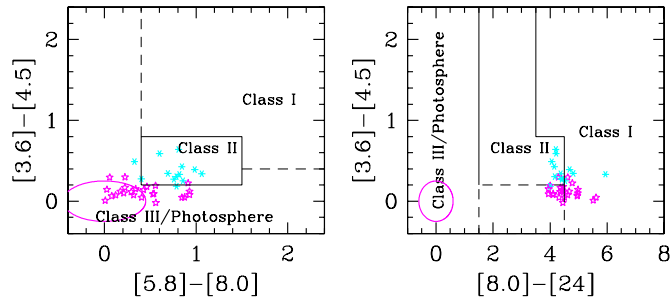


Figure 7. Distribution of objects with transition disks (star marks) or with pre-transition disks (asterisks). In the left panel, objects with transition disks are more concentrated near the locus of Class III/Photosphere objects, but on the right they are located around the border between Class I and II.

(A color version of this figure is available in the online journal.)

in the C–C diagrams are shown in Figure 7. In the ($[3.6] - [4.5]$, $[5.8] - [8.0]$) diagram, objects with pre-transition disks are located in the Class II locus, but most of the objects with transition disks are found in the Class III/Photosphere locus or around that. But in the ($[3.6] - [4.5]$, $[8.0] - [24]$) diagram, such classes show strong $24 \mu\text{m}$ excess emission and often fall on the border between Classes I and II. As already noted by Lada et al. (2006), these are the objects with the largest contrast between inner and outer disk emissions and possibly the disks with inner holes. The objects with pre-transition disks may be YSOs with two disks with a gap between the inner and outer disks (see Figure 4 of Espaillat et al. 2008).

Interestingly, more than half (7 out of 13) of the objects with pre-transition disks are in the Spokes cluster—the youngest region (see Section 4.2) in NGC 2264—and therefore the pre-transition disks occur in an early stage of disk evolution. In addition, 18 out of 24 objects with transition disks are in the halo region of the Cone nebula (Cone (H) in Section 4.1) and the Halo region. The fraction is about 29% relative to Class I and II objects in the Cone (H) region and about 14% in the Halo region. Furthermore, these objects (see Figure 9) are strongly concentrated between $I_C = 13$ and 16 in the PMS locus, corresponding to masses of about 1 solar mass (see Section 5 for details) at an age of about 3 Myr (Sung et al. 2004). This

suggests that the inner disks of at least some solar mass stars evaporate rapidly and an inner hole is being created at this epoch.

We also classified objects with PAH emission features. When $\log \lambda F_\lambda$ at $[8.0]$ exceeded the line drawn between $[5.8]$ and $[24]$ by at least 0.2 dex and the difference was greater than 3 times the error in λF_λ at $[8.0]$, we classified the object as having a PAH feature. A total of nine such objects were identified. One of them, W90 (= S2144 = SST9597), is a well-known Herbig Be star. S2975 (= SST12833) also showed emission in $H\alpha$ and must also be a Herbig Ae star. Our $H\alpha$ photometry suggests that there is no detected $H\alpha$ emission for SST10184 (= C30920+C30962, C30920 dominates the light). This new BMS star is about 0.5 mag fainter than the lower envelope of the PMS locus and is a Class II object. Although two objects (SST 11099, 10914) have no optical counterparts, they are probably embedded massive YSOs as they are in active SFRs (SST 11099 is in the Spokes cluster and SST 10914 in the Cone (C) region). We could find no optical counterparts for the other four objects. They are relatively faint ($[3.6] > 15$ mag) and probably are SFGs with PAH emission.

We present two CMDs in Figure 8. In this figure, and the next two figures, the YSO classes used are those from our Q_{CC} scheme. In the $[3.6]$ versus $[3.6] - [4.5]$ diagram, Class I (big red dot) and Class II (green square) objects are well separated with few exceptions, but in the $[3.6]$ versus $[5.8] - [8.0]$ diagram, the separation is not evident. The $[3.6] - [4.5]$ color of objects with (pre-)transition disks (see Section 3 for the classification scheme) is close to that of normal objects without disks. But they are redder in $[5.8] - [8.0]$ than normal stars. In the second CMD, we can see many external galaxies (black diamonds) in the faint, red portion of the diagram (identified as galaxies via examination of our deep CFHT images). There is a very bright galaxy (SST 6262 = C22243 = 2MASX J06402351+0956312; $[3.6] \sim 11$ mag). It is apparently an edge-on spiral galaxy (Type in NED: IrS).

We present an I_C versus $(R-I)_C'$ diagram⁸ in Figure 9. Most Class II objects are located along the PMS locus. Some Class II

⁸ $(R-I)_C'$ is $(R-I)_C$ corrected for the effect caused by use of the Mould R filter mentioned in Sung et al. (2008).

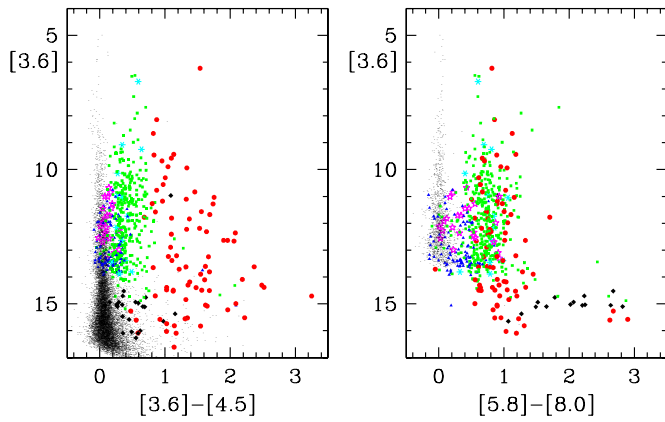


Figure 8. CMDs. Large (red) dot, (green) square, and (blue) triangle represent Classes I, II, and II/III, respectively. (Black) diamonds in the lower part are visually confirmed galaxies. Small dots are objects that do not show any evident excess emission in *Spitzer*/IRAC passbands, while (magenta) star symbols and (cyan) asterisks represent objects with transition disks and pre-transition disks, respectively.

(A color version of this figure is available in the online journal.)

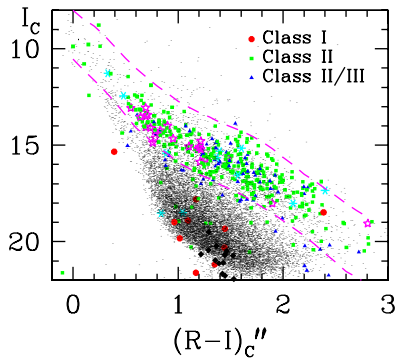


Figure 9. I_c versus $(R-I)_c''$ CMD of stars detected in the *Spitzer*/IRAC photometry. The dashed lines represent the locus of PMS stars in NGC 2264 (Sung et al. 2008). Other symbols are the same as in Figure 8. Most Class I objects except one (C35527) are fainter and bluer as are external galaxies. In general, most Class II objects are well located along the PMS locus of NGC 2264 (see Sung et al. 2008) but there are a non-negligible number of Class II objects found below the PMS locus.

(A color version of this figure is available in the online journal.)

objects are located below the PMS locus and are BMS stars. On the other hand, the few Class I objects with optical photometry are, on average, relatively fainter and bluer than Class II objects. The extragalactic objects also tend to be very faint and thus lie below the PMS locus. Interestingly, many objects with transition disks (star symbols in Figure 9) are concentrated between $I_c = 13$ and 16.

We present the combined 2MASS–IRAC C–C diagrams in Figure 10. The solid and dashed lines represent the locus of reddened or unreddened normal stars. The region between the dashed and dotted lines is the locus of (reddened or unreddened) late-M-type stars. Disked stars are well separated from normal stars at the longer wavelengths, but many of them do not show an appreciable IR excess in the $(J-H, K_s - [3.6])$ diagram and are located in the region occupied by late-M-type stars. One Class I object C35527 does not show any excess emission in this diagram. This may be due to variability of the object (see Figure 6 and Section 6.3.2). There is no clear separation between Class I and II objects in the figures, at least in terms of $J-H$ excess. This fact implies that the size of the near-IR excess is not strongly related to the evolutionary stage of YSOs. Few Class

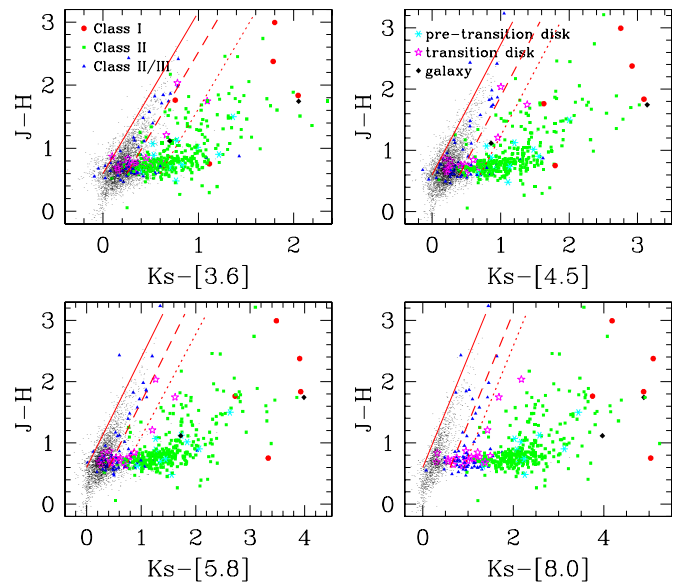


Figure 10. $(J-H, K_s - [IRAC])$ C–C diagram. The solid and dashed lines in the diagrams represent, respectively, the apparent blue and red ridge of normal (reddened or unreddened) stars. The region between the dashed and dotted line denotes the locus of (reddened or unreddened) late-M-type stars. The meaning of the symbols is explained in the upper two panels.

(A color version of this figure is available in the online journal.)

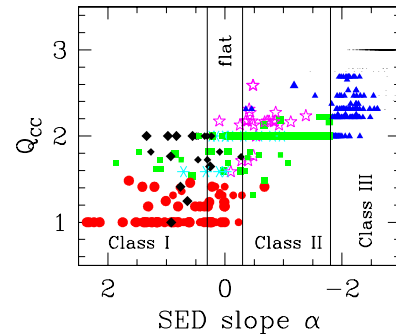


Figure 11. Comparison of the SED slope and photometric criterion Q_{CC} . Symbols are the same as in Figure 8. In general, the two criteria correlate well.

(A color version of this figure is available in the online journal.)

I objects appear in these diagrams because most of the Class I sources are too faint to be detected at J by the 2MASS.

3.3. Final Classification and Comparison

The photometric classification criteria Q_{CC} are compared with the SED slope α in Figure 11. In general, Q_{CC} is well correlated with the slope α . There are several exceptions. One is W90 (= S2144 = SST 9597). As can be seen in Figure 6, the slope α of W90 is +0.56, suggesting that the star is a Class I object. But originally a Class I object was a YSO in the early evolutionary stage, that is, a YSO with an accretion envelope. In this respect, W90 is not a Class I object. We kept the photometric classification for W90. If the two criteria conflicted, in general we adopted the later evolutionary stage. In many cases, such conflicts were caused by errors in the SED slope. Some of the objects have properties that are very close to the border between Classes I and II in Figure 12—their actual classification is therefore somewhat ambiguous.

We also compare the results from the two classification schemes in Figure 12. The symbol type represents the class from the SED slope, while the color denotes the class from

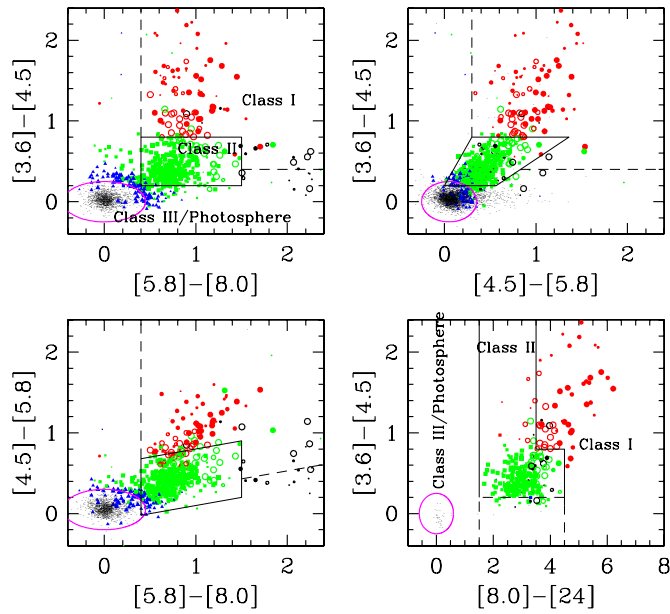


Figure 12. Comparison of SED slopes and photometric classification criteria. The color represents the class from photometric criteria, while the symbols denote the class from the SED slope. The size of the symbols is inversely proportional to the error in the SED slope. The color of symbols is the same as in Figure 8. Filled circles, open circles, squares, and triangles, respectively, represent Class I, flat, Class II, and Class III objects.

the photometric criteria. The size of the symbols is inversely proportional to the error in α . We did not mark objects with pre-transition or transition disks. As can be seen in Figure 12, the two results match quite well. The objects with flat spectra (open circles) are scattered along the border line between Classes I and II. Photometric Class II objects with flat spectra are distributed in the red part of the Class II locus. Class II/III objects are distributed around the outer boundary of the Class III/Photosphere objects. The YSO class from our final classification is listed in the 20th column of Table 1.

An aim of this study was to obtain the fraction of stars with disks. To do that, we need to identify a subset of the NGC 2264 population where we believe to have a nearly complete list of members. We believe that the best choice for this is the S MON and CONE regions of Sung et al. (2008), where our membership completeness was very high. We only consider stars in the PMS locus ($I_C = 8-15.5$). $I_C = 15.5$ was set from the 80% completeness of all IRAC channels as mentioned in Section 2.3. Among 137 known CTTs, 76 were Class I or II (objects with primordial disks) and 22 were Class II/III (objects with optically thin disks). The disk detection fraction for CTTs was 71.5% (the primordial disk fraction counting only the Class I or II objects was 55.5%). There are 181 objects in the region originally classified as WTTs based on the fact that they are believed to be members but have weak or undetected $H\alpha$ emission. Of these 181 classified as WTTs based on $H\alpha$, we find that 14 objects are Class II based on their IR excesses and 10 are Class II/III objects. The disk detection fraction of WTTs was 13% and the fraction of objects with primordial disks was only about 8%. Two objects were newly identified PMS stars in NGC 2264 from *Spitzer* observation alone. Cieza et al. (2007) obtained about 20% for the primordial disk fraction of WTTs in Ophiuchus, Lupus, and IC 348, while Lada et al. (2006) found that about 12% of the optically classified WTTs in IC 348 had primordial disks. On the other hand, Padgett et al. (2006) obtained a much lower disk fraction of about 6% for

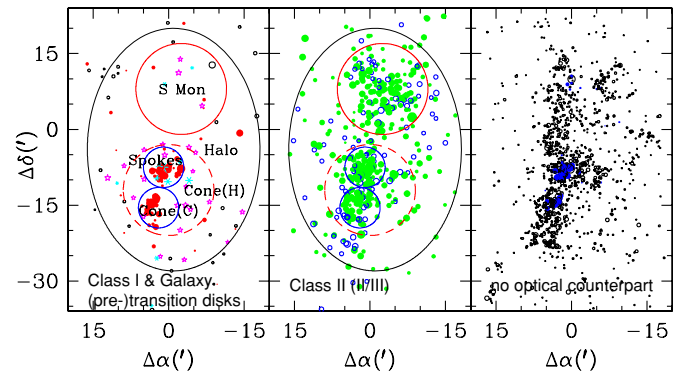


Figure 13. Left: the spatial distribution of Class I objects (red dots) and optically confirmed galaxies (open circles). Asterisks and stars represent, respectively, objects with pre-transition disks and with transition disks. Middle: the distribution of Class II (green dots) and II/III objects (blue circles). Right: the distribution of optically invisible IR sources. Blue dots represents X-ray emission objects with no optical counterpart.

relatively isolated WTTs. Our value for NGC 2264 is between these extremes. For all PMS objects (CTTs plus WTTs), our disk detection fraction is 38%.

4. DISTRIBUTIONS OF YOUNG STELLAR OBJECTS

4.1. Spatial Distributions

The spatial distribution of YSOs contains information about both where they are formed and what happens after that due to dynamical evolution. Based on the density distribution of $H\alpha$ emission stars, two active SFRs (S MON and CONE) and the HALO region surrounding these two subclustering were identified in Sung et al. (2008). Mid-IR images obtained with the *Spitzer Space Telescope* give invaluable information on the embedded YSO population. The spatial distribution of YSOs in NGC 2264 is shown in Figure 13. Most Class I objects are concentrated in either the Spokes cluster ($\Delta\alpha = 1'.0$, $\Delta\delta = -7'.5$) or the Cone nebula region ($\Delta\alpha = 2'.0$, $\Delta\delta = -15'.5$ —Cone (C)). These two subclustering belong to the CONE region as defined in Sung et al. (2008). The Class II objects are more widely distributed, but the distribution of Class II objects definitely resembles the distribution of $H\alpha$ emission stars in Sung et al. (2008). Now, based on the spatial distribution of YSOs detected from *Spitzer* observation, the definition of the SFRs should be refined. The CONE nebula region in Sung et al. (2008) should be divided into three regions—the Spokes cluster (Teixeira et al. 2006), the Cone (C) (C means “core”), and Cone (H) (H means “halo”) regions. The spatial distribution of pre-transition disks and transition disks is shown in the left panel of Figure 13. The other regions are the same as in Sung et al. (2008). The one bright Class I object in the HALO region is C13507 (= SST 2558 = R04-45; see Section 2.5). Reipurth et al. (2004) classified the object as being of $H\alpha$ emission class 4.5 (prominent in $H\alpha$).

In the right panel of Figure 13, we plot the spatial distribution of IR objects with no optical counterpart. Blue dots represent X-ray emission objects (see Section 2.3). Interestingly, most X-ray sources without optical counterparts are coincident with the location of the two embedded clusters. This fact favors our contention that these objects are bona fide members of the two embedded subclustering. The other X-ray emission sources surround the most massive star S Mon. The optical counterpart of these objects may not be detected in deep optical images due to the scattered light from S Mon—the optically brightest star in NGC 2264 (e.g., PID 165 in Table 3 of Sung et al. 2004).

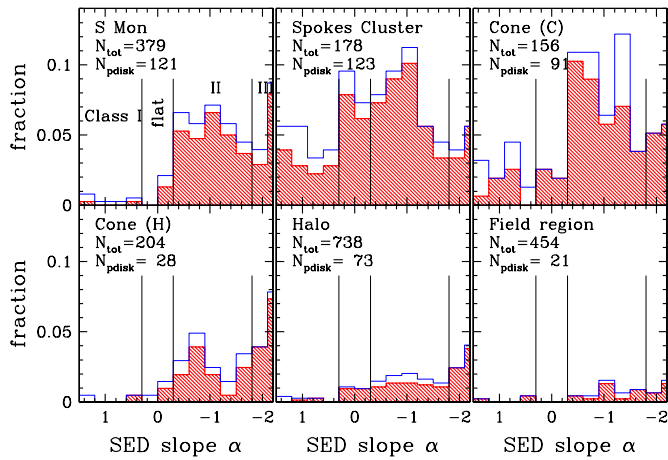


Figure 14. Distributions of the SED slope α for all objects in a given region. The hatched histogram represents the fraction of α with a small error, while the white histogram denotes the fraction of α regardless of error. N_{tot} represents the total number of objects having good data in the region, while N_{pdisk} means the number of objects having $\alpha \geq -1.8$. For the S Mon region, Class II objects are dominant. The fraction of Class I objects is high in the Spokes cluster. Cone (C) is intermediate between the Spokes cluster and S Mon. The other three regions are dominated by Class III/Photosphere objects.

(A color version of this figure is available in the online journal.)

4.2. Frequency Distributions of Spectral Energy Distribution Slopes

The distribution of SED slopes for a given SFR can give information on the evolutionary stage of the SFR. Figure 14 shows the distribution of all objects (detected in at least four IRAC bands and where the total error in the four IRAC bands is less than 0.25 mag) in a given SFR, while Figure 15 represents that of optically visible objects in the SFRs. The hatched histogram represents the distribution of α with smaller error ($\epsilon(\alpha) \leq 0.3$), while the open histogram denotes the distribution of all samples.

The distribution of α is far different in the upper three panels. Class II objects are dominant in the S Mon region, while the fraction of Class I and flat spectrum objects is very high in the Spokes cluster. Cone (C) is intermediate between these two regions. Most of the Class I objects are invisible down to $I_C = 22$ mag, that is, embedded objects. These facts imply that the Spokes cluster is the youngest and S Mon is the oldest. The average values of α for $\alpha > -2.5$ are -1.31 , -0.51 , and -0.80 for S Mon, the Spokes cluster, and the Cone (C) region, respectively. (If the whole range of α is considered, then the average values of α are -2.01 , -0.84 and -1.67 for S Mon, the Spokes cluster, and the Cone (C) region, respectively.) If we accept the gradual evolution of SEDs, the difference in the mean value of α among subclusterings also demonstrates the sequence of star formation within NGC 2264. Although there are several embedded Class II objects in the Spokes cluster, the physical connection between the embedded and exposed population (in Figure 15) is unclear. The continuous distribution of α and the spatial concentration of both Class I and II objects in the Spokes cluster may imply a physical connection between the embedded population and the exposed population. In addition, Rebull et al. (2007) recently found several young stellar aggregates with a wide range of SEDs in the Perseus SFR.

The other three regions in the lower panel are dominated by Class III/Photosphere objects. Interestingly, the peak of the distribution occurs at $\alpha = -2.75 \pm$ (Halo: 0.19, Field: 0.16).

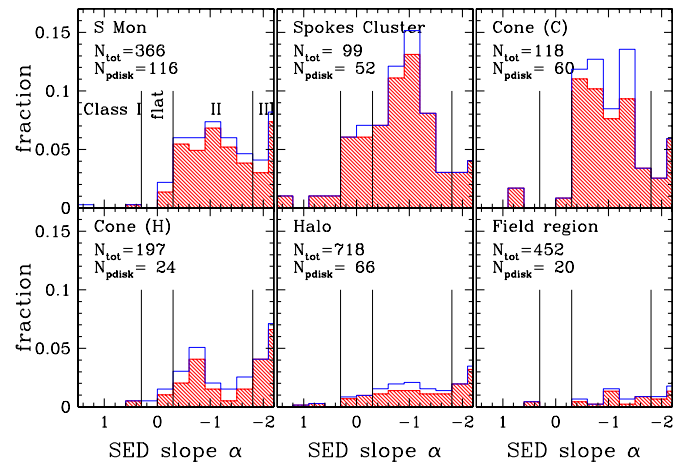


Figure 15. Distributions of slope α of optically visible objects. Symbols are the same as in Figure 14.

(A color version of this figure is available in the online journal.)

This value is very close to the expected value of α ($\alpha \approx -2.8$ for an average over stellar spectral types—Harvey et al. 2006). In NGC 2362 ($A_V = 0.3$ mag), the peak distribution of stars without disks occurs at $\alpha = -2.85 \pm 0.17$ (Dahm & Hillenbrand 2007). In IC 348 and Taurus SFR, the peak frequency of α occurs at about -2.7 (Lada et al. 2006). The slight difference in α of the peak distribution among young open clusters could be interpreted as a difference in reddening as the SED slope is affected by reddening.⁹

5. DISK FRACTION

The frequency and lifetime of disks around young stars are important topics of recent research because planets are believed to form in the disks. The lifetime of a disk should be at least longer than the time required for planet formation. In addition, the frequency of long-lived disks should be consistent with the frequency of exoplanets in the solar neighborhood. From a survey of several young open clusters in the L band, Haisch et al. (2001) concluded that the initial disk fraction is as high as 80% and that the disk fraction decreases rapidly with a half-lifetime of about 3 Myr. They found that about 50% ($\pm 10\%$) of stars in NGC 2264 showed a $JHKL$ excess. Lada et al. (2006) estimated the total frequency of disk-bearing stars in the 2–3 Myr old young open cluster IC 348 to be $50\% \pm 6\%$ and that of stars surrounded by primordial disks to be $30\% \pm 4\%$. Recently, Dahm & Hillenbrand (2007) determined a low value ($\sim 7\% \pm 2\%$) for the primordial disk fraction in the 5 Myr old young open cluster NGC 2362. As the age of NGC 2264 is about 3 Myr (Sung et al. 2004), information on the disk fraction will be valuable data for the disk evolution and the lifetime of primordial disks around young stars.

We present the disk fraction of stars in the PMS locus of NGC 2264 as a function of stellar mass in Figure 16. As the membership selection is fairly incomplete in the HALO and FIELD regions of Sung et al. (2008), we consider only the member stars in the S MON and CONE (Spokes + Cone (C) + Cone (H)) regions. The mass of PMS members in the PMS locus of NGC 2264 (see Figure 9) is derived using the PMS

⁹ The amount of reddening can alter the slope by $d\alpha/dE(B-V) \propto 0.0224 \text{ mag}^{-1}$ for the reddening law adopted in Section 3.2. If we assume that the difference in α ($\equiv \alpha_{\text{peak}} - \alpha_{\text{expected}} \approx -0.05$) is solely caused by reddening, the derived reddening is about $E(B-V) \approx 2.2$ mag.

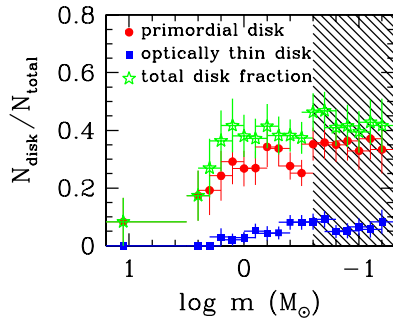


Figure 16. Disk fraction of stars in NGC 2264. The mass of PMS stars is estimated using the PMS evolution models of Siess et al. (2000) and Baraffe et al. (1998) for very low-mass stars. (Red) Dots and (blue) squares represent the minimum fraction of stars with primordial disks and with optically thin disks, respectively. The bar represents the error from Poisson statistics. The stars represent the total disk fraction, that is, the sum of primordial disks, optically thin disks, pre-transition disks, and transition disks. The hatched portion represents the range where membership selection is incomplete.

(A color version of this figure is available in the online journal.)

evolution model of Siess et al. (2000) for mass $> 0.1 M_{\odot}$ and using Baraffe et al. (1998) for lower mass stars. Because the mass determinations require optical photometry, the set of stars we consider excludes the youngest, most embedded members, especially in Spokes and Cone (C). The theoretical parameters are transformed to the observational CMD using the empirical color–temperature relation for late-type stars of Bessell (1995). The distance ($V_0 - M_V = 9.4$ mag) and reddening ($E(B - V) = 0.07$) are from Sung et al. (1997). The fraction of primordial disks is the ratio of the number of Class I and Class II stars to the total member stars for a given mass range. The fraction of optically thin disks is that of Class II/III stars to the total number of member stars. For clarity in the figure, we did not mark the fraction of pre-transition and transition disks. But the total disk fraction is the ratio of all disked stars (primordial disk + optically thin disk + pre-transition disk + transition disk) to total member stars for a given mass range. The disk fraction presented in Figure 16 was derived in logarithmic mass intervals of $\Delta \log m = 0.2$ for $\log m < 0.5$ and then recalculated using the same bin size but shifted by 0.1 in $\log m$ to smooth out the binning effect. The hatched area represents the region where membership selection is somewhat incomplete.

The fraction of stars with a primordial disk is about 28.5% for $\log m = 0.2$ to -0.5 and slightly higher (about 35%) for $\log m = -0.2$ to -0.3 . The fraction of optically thin disks is generally very low, but slightly higher for low-mass stars. The total disk fraction is, on the other hand, nearly constant (about 38%) between $\log m = 0.3$ and -0.6 . Interestingly, the fraction of transition disks is very high in the range $\log m = 0.1$ to -0.1 (about 8.5%). This fact suggests that at the age of the non-embedded population of NGC 2264 (about 3 Myr—Sung et al. 2004) disk evaporation, especially the inner disk, of solar mass stars is very active. If we include the fraction of pre-transition disks and transition disks to the fraction of primordial disks, and consider them all as a fraction of the primordial disks, then the disk fraction of solar mass stars is slightly higher than that of lower-mass stars.

6. EFFECT OF MASSIVE STARS ON DISKS

6.1. Disk Fraction of Young Stars around S Monocerotis

The idea that the formation of massive stars could influence the fate of natal clouds as well as its low-mass siblings can be

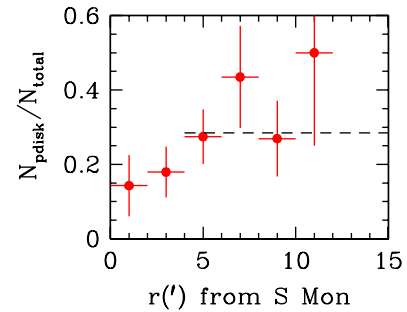


Figure 17. Radial variation of the primordial disk fraction from S Mon. The thin lines represent the errors from Poisson statistics. The meaning of the other symbols is the same as Figure 16.

(A color version of this figure is available in the online journal.)

traced back to the paper by Herbig (1962). *HST* images of the Orion nebula have clearly revealed the effect of the massive star θ^1 C Ori (O6pec) on surrounding low-mass young stars, especially the protoplanetary disks around them (O’Dell & Wen 1994). Recently, Sung et al. (2008) showed that the strength of $H\alpha$ emission $\Delta(R'_C - H\alpha)$ decreases systematically with an increasing distance from the massive star S Mon (O7V) or HD 47887 (B1.5Vp). In addition, the ^{13}CO map of NGC 2264 (Fűrész et al. 2006) shows a bubble-like feature at the position of the most massive star S Mon.

It is important to look for clues related to the effect of massive stars on the fate of the disks around low-mass stars. We calculated the variation of disk fraction as a function of distance from the most massive star, S Mon; the result is shown in Figure 17. In the calculation, we used data for stars with masses between $\log m = 0.3$ and -0.6 to minimize effects due to incompleteness in the data. Interestingly, the fraction of primordial disks increases as the distance from S Mon increases and approaches the average value of primordial disk fraction at $r \approx 6'$. [$N_{\text{pdisk}}/N_{\text{total}} \approx 0.100 (\pm 0.030) + 0.033 (\pm 0.009) r'$, $r = 0.97$ for $r \leq 5.6$]. In addition, there is no disked star within $r = 1'$. These observations strongly suggest that the ultraviolet photons and stellar wind from the massive O7V star S Mon has actually affected the fate of the primordial disks around young low-mass stars up to $d \approx 1.2$ pc. Recently, Balog et al. (2007) found a similar trend in NGC 2244. We also checked for variation in disk fraction with distance from the second most massive star, HD 47887 (B1.5Vp), but found nothing.

6.2. Disk Fraction Versus Age Relation

Prior to *Spitzer*’s launch, Haisch et al. (2001) performed an *L*-band survey of young open clusters and derived the half-lifetime for disks around young stars. Because the disk lifetime is a function of stellar mass (Lada et al. 2006; Dahm & Hillenbrand 2007), the disk fraction versus age relation could be affected by the limiting magnitude of the survey. Now the primordial disk fractions based on *Spitzer* observation have been calculated for more than a dozen of young open clusters and associations. The *Spitzer* version of the ‘‘Haisch’’ diagram has already been determined (e.g., see Hernández et al. 2007a). However, there are several reasons for re-examining the relation. In many cases, the mass range was not taken into account; in addition, membership selection seems to be incomplete because many researchers calculated the disk fraction based on the members selected from *Spitzer* observations only. In that case, many young stars without detectable excess emission in the mid-IR may have escaped membership selection.

6.2.1. NGC 1333 and Serpens

Gutermuth et al. (2008) presented the background-subtracted K_s luminosity function for the young embedded cluster NGC 1333. The fraction of IR excess YSOs of bright K_s objects is slightly higher than that of fainter low-mass objects. The fraction of IR excess stars for $K_s \leq 12.5$ is about 80 (± 16)%, while that of low-mass stars ($K_s = 10.5\text{--}12.5$, equivalently $m = 0.2\text{--}1.0 M_\odot$) is about 73 (± 16)%. Such a difference in the objects with disks could be caused by the problem in statistical subtraction due possibly to spatially varying reddening, and therefore we adopt 80% as the primordial disk fraction of NGC 1333. Another young embedded star-forming core Serpens was studied by Winston et al. (2007) with the data from the *Spitzer Space Telescope* and *Chandra*. They used the criterion of Class II objects as the SED slope α between -2.0 and -0.3 . For the completeness of membership selection, we limit our analysis to objects within the *Chandra* FOV. In addition, for the consistency of classification used in this paper, we exclude six objects with $\alpha < -1.8$ or a larger error in the SED slope. In addition we only calculate the primordial disk fraction of YSOs brighter than $K_s < 12.6$. The fraction is only about 1% lower than that of all members in the *Chandra* FOV.

6.2.2. NGC 2244

The young open cluster NGC 2244 is one of the important targets for studying the effect of massive stars on the evolution of disks around low-mass stars because it contains about 30 early-type stars between O5V and B3V. Park & Sung (2002) performed optical photometry and determined the distance and age. Later, Balog et al. (2007) found 25 Class I and 337 Class II objects in the cluster based on *Spitzer* observation and obtained a slightly lower disk fraction of about 45% for YSOs in NGC 2244.

Recently, Wang et al. (2008) studied the cluster using data obtained with *Chandra*. They found over 900 X-ray sources in the cluster. We have reanalyzed the cluster using the optical images of Park & Sung (2002), *Spitzer* data in Balog et al. (2007), and X-ray sources in Wang et al. (2008). For completeness of membership selection, we limit our attention to the overlap region of the three observations. For X-ray observations, we limit the FOV to that of *Chandra* ObsID = 3750 because the exposure times of other regions were much shorter. There were 748 members in the region. Among them 204 stars have masses between $1 M_\odot$ and $0.5 M_\odot$ (the completeness limit of X-ray-selected members), with 74 stars being classified as Class I, flat, and Class II. The fraction of stars with primordial disks is about 36 (± 5)%. This value is slightly lower than that obtained by Balog et al. (2007). The median age of the low-mass stars is 1.7 (± 0.2) Myr.

6.2.3. Ori OB1 Association

Hernández et al. (2007a) studied the disk fraction of about 3 Myr old open cluster σ Ori and obtained a disk fraction of about 35% for T Tauri stars. They listed 336 members, but many of them do not show variability or X-ray emission. We selected 194 members based on X-ray emission, IR excess, and optical variability. Among 194 members, 99 objects have masses between $1 M_\odot$ and $0.2 M_\odot$; among these 99 low-mass stars, 48 are classified as Class II or YSOs with (pre-)transition disks. The primordial disk fraction of σ Ori is about 48%. There are no homogeneous optical data for the cluster, and therefore it is very difficult to determine the median age of the

cluster. Various optical data in their tables and from SIMBAD database were compiled, and the median age was estimated to be 1.9 (± 0.3) Myr from the (V , $V - I$) diagram.

The disk fraction of the 25 Ori region was studied by Hernández et al. (2007b). They listed 115 members. Among them, 54 stars have masses between $1 M_\odot$ and $0.2 M_\odot$ ($Sp = K7 - M4$ or $J = 12\text{--}13.2$). Only one star is classified as Class II. Normally the age of 25 Ori is assumed to be about 10 Myr, but Figure 4a of Briceño et al. (2007) implies a slightly younger age. We adopt the age of 25 Ori as 8 (-1 , $+2$) Myr. NGC 2068/2071 is another young SFR in the Ori OB association. Flaherty & Muzerolle (2008) presented *Spitzer* data, spectral type, and stellar parameters of 69 likely members. Among 69 likely members, 48 stars are low-mass stars ($Sp = K7 - M4$) and 26 out of 48 stars are classified as CTTS. Therefore, the primordial disk fraction of NGC 2068/2071 is about 54%.

6.2.4. IC 348 and NGC 2264

The young open cluster IC 348 in the Perseus SFR has been well studied by Lada et al. (2006). They listed 307 members selected from X-ray emission, IR excess, and spectroscopy. The number of low-mass members between K7 and M4 is 108, and 37 out of 108 stars are classified as stars with thick disks. The primordial disk fraction of low-mass stars is therefore about 34 (± 6)%. There are three active SFRs in NGC 2264, but many of the YSOs in two of these SFRs (Spokes cluster and Cone(C)) are an embedded population. The mass and age of these YSOs cannot be determined reliably. We calculated the disk fraction of YSOs in the S Mon region of NGC 2264. The completeness limit of membership selection was set by the exposure time of the X-ray observations (see Sung et al. 2004; Ramírez et al. 2004). The total number of low-mass members is 139, and among them 37 stars were classified as stars with primordial disks. The median age of low-mass stars in the S Mon region of NGC 2264 is 3.1 Myr.

6.2.5. γ Vel

One of the most important clusters in this study comprises the young stars around the WC star γ Vel. Hernández et al. (2008) found several debris disk candidates among 579 candidate members based on the CMDs. We have reanalyzed their photometric data and adopted a more conservative set of membership criteria. The number of members we find from X-ray emission and IR excess is only 141 stars. Among them, 41 stars are low-mass stars ($\log m = 0.0$ to -0.7) with only one Class II object. The age of the cluster was assumed to be about 5 Myr (Hernández et al. 2008), but the median age of our selected members is 3.4 (± 0.5) Myr. Jeffries et al. (2009) also obtained a similar age for γ Vel. The primordial disk fraction of γ Vel is therefore about 2 (± 2)%, which is far lower than any other similar age young SFRs.

6.2.6. Cep OB2 Association

There are two young open clusters (Tr 37 and NGC 7160) in Cep OB2 association. Tr 37 is younger, and its assumed age is about 4 Myr (Sicilia-Aguilar et al. 2006) while that of NGC 7160 is about 10 Myr. Sicilia-Aguilar et al. (2005, 2006) selected spectroscopic members and studied the young stars in these clusters. There are 130 and 14 low-mass members ($Sp = K7 - M4$) in Tr 37 and NGC 7160, respectively. Among 130 low-mass members in Tr 37, 63 stars are of Class II or stars with transition disks. The median age of Tr 37 in Table 2 of Sicilia-Aguilar

et al. (2006) is 2.6 Myr. The fraction of primordial disk is about $49 (\pm 7)\%$. This value is slightly higher than other clusters of a similar age. However, there are some active regions of current star formation in this region (IC 1396A and IC 1396N), near the O6V star HD 206267. This indicates that there are stars with a spread of age in this region, which could bias the disk fraction to higher values or, equivalently, where the age based on optical photometry could be older than the average age of all the young stars in the region (because the youngest stars are embedded). In NGC 7160, only 1 star among 14 low-mass members is classified as a CTTS.

6.2.7. NGC 2362 and Upper Scorpius

The frequency of disked stars in the young open cluster NGC 2362 is well studied by Dahm & Hillenbrand (2007). They selected members from X-ray observation and spectroscopy. There are 168 low-mass members among 232 members, and only 13 out of 168 stars have primordial disks. The age of NGC 2362 is assumed to be 5 Myr, but a slightly younger age is more favored from their Figure 2. We adopt the age of the cluster as $4 (\pm 1)$ Myr. Carpenter et al. (2006) published *Spitzer* IRAC 4.5 μm , 8.0 μm , and intensified Reticon spectrograph (IRS) 16 μm data for 204 stars in the Upper Scorpius (Upp Sco) OB association. Among them 85 stars belong to the low-mass regime, and 12 out of 85 low-mass stars show an IR excess. The fraction of IR excess stars is about $14 (\pm 4)\%$. This value is slightly higher than that of NGC 2362. This could result from selection effects because Upp Sco is a part of Sco-Cen OB association and therefore the membership selection of low-mass stars could be biased toward X-ray bright stars for the surveyed regions.

6.2.8. η Cha

η Cha is an interesting young stellar group of age $6 (-1, +2)$ Myr (Luhman & Steeghs 2004). There are 18 known members in the group and seven are low-mass stars (Sp = K7 – M4). Among seven low-mass stars, two stars show an excess emission from *Spitzer* observation. Although the fraction of stars with the primordial disk is very high (about $29\% \pm 23\%$), the number of member stars is very small. In addition, the spectral type of the earliest star η Cha is B8V, and the UV radiation field is therefore far weaker than that of the other SFRs discussed here. The group is far away from the galactic disk. Such differences in environment could affect the lifetime of disks of stars in η Cha.

6.2.9. Disk Fraction Versus Age

The Taurus-Auriga SFR is another of the important SFRs that has been observed with *Spitzer* IRAC (Hartmann et al. 2005). We did not try to reanalyze YSOs in Tau SFR because Tau SFR can be subdivided into several small SFRs that may have different star formation histories. The primordial disk fraction and age of each cluster are summarized in Table 4 and are drawn in Figure 18.

Figure 18 shows that the primordial disk fraction of NGC 2244 and γ Vel is slightly lower than the other clusters for a similar age. And although the most massive O7V star in NGC 2264 S Mon may affect the disks of low-mass stars around the star (see Section 6.1), the overall disk fraction seems to be not affected strongly by the presence of the O7V star (about $30 M_{\odot}$). In addition, for older clusters (age ≥ 6 Myr) the fraction of primordial disks is very low, but not zero. Several H α emission stars can be found in the 7.5 Myr cluster NGC 6531 (M21) (Park et al. 2001).

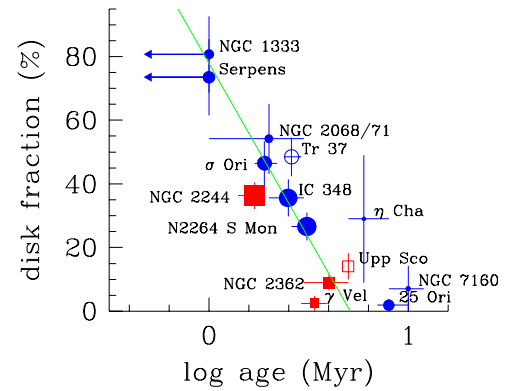


Figure 18. Disk fraction vs. age diagram. The primordial disk fraction of young open clusters and groups is calculated for low-mass stars ($m \leq 1 M_{\odot}$) down to the completeness limit of membership selection. A square represents the clusters containing stars with the earliest spectral type of O7 or earlier or with evolved similar massive stars. The solid line represents the relation between the primordial disk fraction and age of clusters younger than 6 Myr. We used a weighted regression (weight = square root of the number of low-mass stars). Half of the normal weight was applied for Tr 37 and Upp Sco (open symbols) due to the reasons mentioned in the text. Two young clusters (NGC 2244, and γ Vel) were omitted from the regression because the disk fraction of these clusters is suspected to be strongly affected by the presence of massive star(s).

(A color version of this figure is available in the online journal.)

The solid line in Figure 18 is the result from a weighted regression. Two young clusters (NGC 2244 and γ Vel) and three old (age ≥ 6 Myr) group and clusters were excluded from the regression. The weights applied were proportional to the square-root of the number of low-mass members, and the weights of Tr 37 and Upp Sco were half of the normal weight because of the reason mentioned above. The regression result is

$$f_{\text{disk}} = 78.0(\pm 2.2) - 110.0(\pm 5.0) \log \text{age (Myr)}.$$

This result implies that the primordial disk fraction at birth is about 80% and the disk lifetime is $5.1 (\pm 0.5)$ Myr. The fraction of primordial disks in NGC 2244 and γ Vel is about 17% lower than other clusters. And that of η Cha is higher than the others. A common disk lifetime of about 5 Myr also indicates that planets should form (or at least mostly form) within this period. The disk lifetimes obtained here are consistent with the values obtained by Strom et al. (1989) from the observation of T Tauri stars in the Tau-Aur SFR.

7. DISCUSSION

7.1. Stars Below the Pre-main-sequence Locus

Herbig (1954) pointed out that the Ae star (or now possibly a Herbig Be star—Pérez et al. 2008) W90 is 3 mag fainter than normal A type stars. Later, Strom et al. (1972) proposed that the location in the CMD could be explained by assuming that it was being viewed through a nearly edge-on circumstellar disk/envelope containing primarily large dust grains. On the other hand, Palla & Stahler (2002) suggested a prolonged period of star formation from the presence of some fainter PMS stars in the CMDs of the Trapezium cluster and the Taurus SFR. Slesnick et al. (2004) found a population of faint PMS stars in the Trapezium cluster whose inferred age would be of the order of 10 Myr if judged directly from isochrone fitting; they concluded that these stars were best explained by the disk obscuration model. From the spatial density distribution and their near-IR excess, Sung et al. (2008) supported the near edge-on disk model of below the PMS locus (BMS) stars.

Table 4
Primordial Disk Fraction of Selected Young Clusters and Stellar Groups

Cluster	Age (Myr)	Sp Type ^a	Disk Fraction (%)	N_{total}^b	N_{LM}^b	N_{disk}^b	Mass Range	Selection Criteria ^c	PMS model ^d	reference ^e
NGC 1333	≤ 1	...	80.7 ± 16.0	≈ 90	57	46	$K_s < 12.5$	IR	BCAH98	1
Serpens	≤ 1	...	74.8 ± 16.1	137	49	36	$K_s < 12.6$	X, IR	...	2
NGC 2244	1.7 ± 0.2	O5V	36.2 ± 4.9	748	204	74	$\log m = 0.0 - -0.3$	X, IR	SDF00	3, 16, 17
σ Ori	1.9 ± 0.3	O9.5V	48.5 ± 8.5	194	99	48	$\log m = 0.0 - -0.7$	X, IR, V	SDF00	4
NGC 2068/2071	2.0 ± 1.0	B1.5V	54.2 ± 13.2	67	48	26	Sp = K7 – M4	Sp	SDF00	5
IC 348	2.5 ± 0.5	B5V	34.3 ± 6.5	307	108	37	Sp = K7 – M4	X, IR, Sp	BCAH98	6
Tr 37	2.6 ± 0.3	O6V	48.5 ± 7.4	172	130	63	$\log m = 0.0 - -0.4$	Sp	SDF00	7, 15
NGC 2264 S Mon	3.1 ± 0.3	O7V	26.6 ± 4.9	327	139	37	$\log m = 0.0 - -0.6$	X, H α , IR, Sp	SDF00	This
γ Vel	3.4 ± 0.5	WC	2.4 ± 2.5	141	41	1	$\log m = 0.0 - -0.7$	X, IR	SDF00	8
NGC 2362	4.0 ± 1.0	O9Ib	7.7 ± 2.2	232	168	13	$\log m = 0.0 - -0.7$	X, IR, Sp	BCAH98	11
Upp Sco	5.0	B8Iab/B0.5V	14.1 ± 4.4	204	85	12	Sp = K7 – M4	Sp	...	12
η Cha	6.0 ± 2.0	B8V	28.6 ± 22.9	18	7	2	Sp = K7 – M4	Sp	BCAH98	9, 10
25 Ori	8.0 ± 1.5	B1Vpe	1.9 ± 1.9	115	54	1	Sp = K7 – M4 or $J = 12 - 13.2$	Sp	SDF00	13, 14
NGC 7160	10 ± 2.0	BIII-III	7.1 ± 7.4	25	14	1	Sp = K7 – M4	Sp	SDF00	7, 15

Notes.

^a Spectral type of the earliest or evolved star.

^b N_{total} : total number of member stars, N_{LM} : number of low-mass stars in the mass range (column 8), N_{disk} : number of stars with primordial disks.

^c X: X-ray emission stars, IR: IR excess stars from *Spitzer* observation, H α : H α photometry, Sp: spectroscopically confirmed members.

^d BCAH98: Baraffe et al. (1998); SDF00: Siess et al. (2000).

^e (1) Gutermuth et al. 2008; (2) Winston et al. 2007; (3) Wang et al. 2008; (4) Hernández et al. 2007a; (5) Flaherty & Muzerolle 2008; (6) Lada et al. 2006; (7) Sicilia-Aguilar et al. 2006; (8) Hernández et al. 2008; (9) Megeath et al. 2005; (10) Luhman & Steeghs 2004; (11) Dahm & Hillenbrand 2007; (12) Carpenter et al. 2006; (13) Hernández et al. 2007b; (14) Briceño et al. 2007; (15) Sicilia-Aguilar et al. 2005; (16) Balog et al. 2007; (17) Park & Sung 2002.

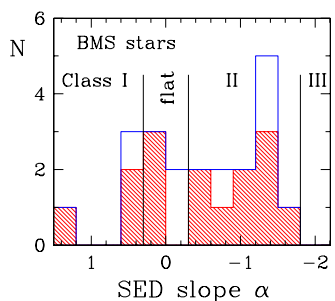


Figure 19. Distribution of the SED slope α of BMS stars.
(A color version of this figure is available in the online journal.)

Sung et al. (2008) presented 82 BMS candidates. Among them, 15 were outside the *Spitzer* field of view, 8 were double in IRAC, 11 were not detected, 2 were detected only in [3.6], and 22 were detected only in [3.6] and [4.5]. There were only 24 objects that were detected in three or more channels and whose SED slope α could be calculated reliably. (We force fitted a line to the SED although the data did not meet the criteria mentioned in Section 3.2.) The SED slope distribution of BMS stars is presented in Figure 19. Most of the BMS stars (21/24) were disked stars (Class I, flat, or Class II). Three stars (C39036 = LkH α 71, C35777, and C48145) show the SED of stellar photospheres ($\alpha = -2.6$ to -2.8). Ogura 97 (= C32005 = SST 10710), although the star is not classified as a BMS star in Sung et al. (2008), is a BMS star as H α emission has been detected by Ogura (1984); it is a Class I object. With 21 disks and a total of 59 objects where we could have reliably detected a disk ($82 - 15 - 8$), the fraction of BMS objects with primordial disks is about 36%. This value is slightly higher than the primordial disk fraction of members in the PMS locus. As we did not impose any limitation in brightness, the fraction obtained above is a minimum value. If we restrict BMS membership to those

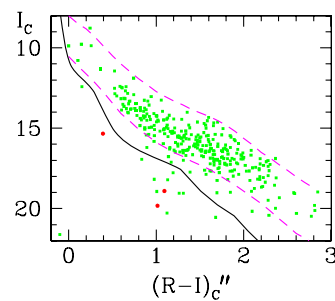


Figure 20. I_c vs. $(R-I)_c''$ CMD of Class II objects and three Class I objects classified as BMS candidates. The dashed lines represent the locus of PMS stars in NGC 2264, while the solid line denotes the reddened zero-age main-sequence relation shifted to the distance of NGC 2264.

(A color version of this figure is available in the online journal.)

candidates with strong H α emission (membership class: “+” or “H”), the fraction increases to about 55% (= 18/33).¹⁰

There are some stars that could be classified as BMS stars (Class I or II) in Figure 9. We list 10 new BMS candidates in Table 5 and draw the CMD of Class II objects and three BMS candidate Class I objects in Figure 20. Three were not listed in Table 12 of Sung et al. (2008) because of small values of ΔI_c ($\Delta I_c < 0.5$ mag), three were too faint ($I_c > 20$ mag), and four had no signature of H α emission. But most of the faint Class I objects are not listed in Table 5 because of their optical images and their spatial location (Field or Halo)—two (SST 3145 and 7707) are too faint to discern whether they are faint stars or galaxies and two (SST 9861 and 21808) are in the vicinity of faint galaxies (see Section 2.5).

¹⁰ As the bright, spatially varying nebulosity in NGC 2264 could affect the quality of photometry, we cannot rule out the possibility of spurious detections of H α emission of some BMS candidates, particularly the fainter ones. Actually the BMS candidates not detected in IRAC or only detected in [3.6] and/or [4.5] are mostly faint ($I_c > 18$ mag for strong H α emission stars and $I_c > 17.5$ mag for weak H α emission stars).

Table 5
New BMS Star Candidates

SST	Sung et al. (2008)	[3.6]	[4.5]	[5.8]	[8.0]	[24]	H α Emission	IR Class	SED Slope	Q _{CC}	ΔI^a
2233	C12598	11.377	10.701	10.245	9.480	6.483	Yes	II	-0.58 ± 0.03	2.0	0.24
6655	C23131	11.377	10.814	10.355	9.703	6.778	Yes	II	-0.69 ± 0.09	2.0	0.45
6892	C23663	13.867	13.286	12.683	11.759	8.431	Yes	II	-0.33 ± 0.13	2.0	4.19
7361	C24781	15.739	14.712	13.378	11.830	7.603	No	I	$+1.35 \pm 0.47$	1.0	2.50
8261	C26827	13.277	12.549	12.063	11.386	8.572	Yes	II	-0.70 ± 0.08	2.0	2.75
10184 ^b	C30920+C30962	13.434	13.302	13.030	10.598	7.672	No	II	-0.04 ± 0.50	2.0	0.51
10710 ^c	C32005	11.773	11.091	9.556	7.853	3.135	?	I	1.34 ± 0.10	1.0	2.58
13708	C36601	14.512	13.759	13.048	12.225		Yes	II	-0.19 ± 0.11	2.0	11.62
18887	C46626	14.028	13.121	12.145	11.107	7.900	No	I	$+0.09 \pm 0.28$	1.3	3.93
21725	C54567	12.666	12.086	11.434	10.716	7.702	Yes	II	-0.55 ± 0.03	2.0	0.30

Notes.

^a Magnitude difference from the faint limit of the PMS locus in NGC 2264.

^b If the actual optical counterpart of SST 10184 is C30962, then SST 10184 may be a SFG with PAH emission. See Section 2.5.

^c Ogura (1984) noted as an H α emission star, but no signature of H α emission from CCD photometry was detected.

The high disk fraction of BMS stars strongly suggests that BMS stars are bona fide YSOs. In addition, a well-known young disked K7 WTTS star KH 15D in NGC 2264 is close to the lower boundary of the PMS locus of NGC 2264 during its bright phase, but becomes a BMS star during eclipse. The star is fainter by about 3.5 mag in I during eclipse, but is bluer by about 0.2 mag in $V-I$ (Hamilton et al. 2005) probably due to the contribution of scattered light. Although the H α emission of KH 15D is not detected photometrically, Dahm & Simon (2005) reported an H α emission equivalent width of 103.1 Å. In addition, the spectra of KH 15D during eclipse do not show any change in spectral type or reddening, indicating that the extinction is caused by larger dust grains (Hamilton et al. 2001; Agol et al. 2004). And the polarization dramatically increased from practically $\sim 0\%$ during out of eclipse to $\sim 2\%$ during eclipse (Agol et al. 2004). In addition, the variation amplitude in [3.6] of KH 15D is nearly the same as that in I_C (see Section 7.2.5), also indicative of gray extinction by large grains. KH15D therefore provides direct evidence in favor of the disk extinction model to explain BMS stars.

7.2. Interesting Objects

7.2.1. W90 (= S2144)

The well-known BMS star W90 (= S2144 = SST 9597) was first found by Herbig (1954) as an emission line A-type star. He also pointed out that it is fainter by 3 mag relative to other PMS stars of a similar spectral type in the cluster. Its PMS nature was confirmed spectroscopically by Strom et al. (1971). From photometric studies, Sung et al. (1997, 2008) found many BMS stars in the cluster. Recently, Pérez et al. (2008) published a vast amount of archival and original photometric and spectroscopic data for W90. They showed the variability and spectral changes of the star.

As mentioned in the previous section, W90 is very red in [5.8] – [8.0]. W90 could be classified as either a Class I or a Class II object. We classified the star as Class II due to its relatively bluer color in [8.0] – [24]. We present the SED of W90 in Figure 6. W90 shows excess emission in the near-IR as well as in all IRAC channels.

7.2.2. C35527—a Class I Object in the PMS Locus

C35527 (= SST 12918; $\alpha_{J2000} = 6^h41^m06^s44$, $\delta_{J2000} = 9^\circ36'58''.6$) is the only Class I object in the PMS locus. The star is 1'.85 SW of KH 15D (see Figure 21), and is barely detected in

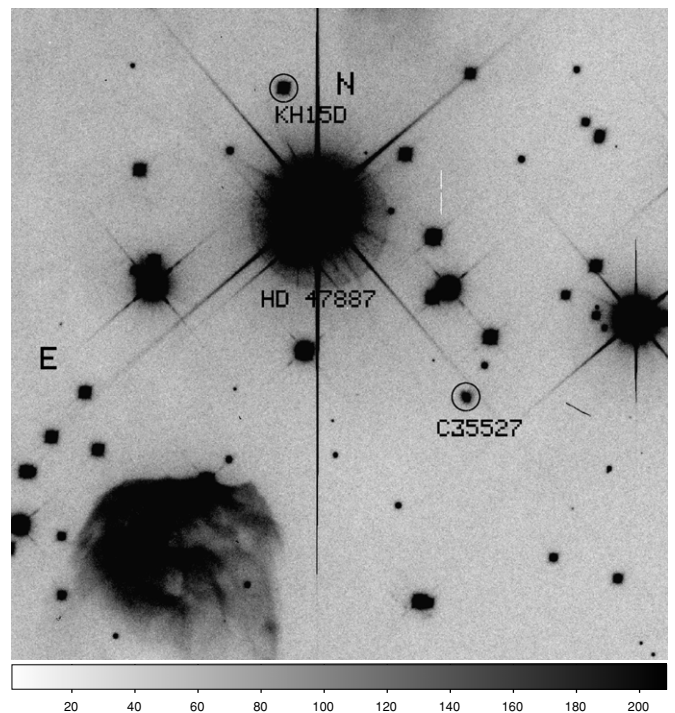


Figure 21. Finder chart of the Class I star C35527. Thin nebulosity can be seen around the star.

the digital sky survey. But in our CFHT images, we can see the object clearly. As can be seen in Figure 21, the star is surrounded by a thin nebulosity. The star is a strong X-ray source (detection significance = 75.05). Its 2MASS colors are those of a highly reddened normal star. Even in $K_s - [3.6]$, the star does not show any signature of an IR excess (Figure 10 (upper left) or Figure 6 (upper right)). This may be caused in part by the variability of the object. But in $K_s - [4.5]$ or longer wavelengths, the star shows an evident IR excess, which increases to a longer wavelength.

The star was detected in our SSO I_C -band image (date of observation: 1997 November 19, UT = 16:15:47.5, MJD = 50771.677627; no “S” ID was assigned). Its I_C magnitude was 17.765 ± 0.068 ($N_{\text{obs}} = 1$). The magnitude and colors from the observation with the CFHT are $I_C = 18.480$, $(R-I)_C^0 = 2.368$, and $(V-I)_C = 5.299$. The star is very red and is variable.

The SED of this star is shown in Figure 6. As there is no direct method to determine the reddening of such a very red

star, we tried to fit the optical $V R_C I_C$ and 2MASS data to a model atmosphere of an effective temperature of 2600 K and surface gravity $\log g = 2.5$. The resulting reddening $E(B - V)$ is about 1.40 mag. The star shows excess emission only in IRAC channels and in $24 \mu\text{m}$.

7.2.3. *FU Ori-Type Candidates AR 6A (= C33859) and AR 6B*

Aspin & Reipurth (2003) suggested that AR 6A (= C33859) is an FU Ori-type PMS star. IRAC colors, including MIPS [24], indicate that the star is a Class II object. From near-IR photometry and spectroscopy, Aspin & Reipurth (2003) estimated the reddening and temperature ($A_V = 18$ mag, $T_{BB} = 3000$ K). Although the star has very red colors ($(R - I)'' = 3.09 \pm 0.02$), the estimated reddening from its SED (see Figure 6) is $E(B - V) \approx 3.65$ mag if we adopt the optical spectral type of the star as G III ($T_{\text{eff}} \sim 5000$ K) suggested from spectral features in the K band. This value is much smaller than the value estimated by Aspin & Reipurth (2003). Such a large discrepancy may be caused by their using limited, near-IR data that are affected by reddening as well as thermal emission, as they have pointed out. In addition, Sung et al. (2008) noted that its location in the near-IR C–C diagram cannot be simply interpreted as the result of reddening.

AR 6B (= SST 11837) was not detected in the deep optical survey of Sung et al. (2008), but the IRAC colors as well as the near-IR photometry of Aspin & Reipurth (2003) suggest that it is a Class I object. The reddening of AR 6B cannot be determined using the near-IR data mentioned above. If we assume the same reddening as that of AR 6A, we cannot fit the SED at all. If we assume $E(B - V) = 0.0$, the blackbody flux of the object is slightly fainter than the detection limit at I_C ($\log \lambda F_\lambda \approx -13.85$ at $I_C = 22$ mag).

7.2.4. *Allen's Source*

Allen (1972) discovered a strong IR source just north of the Cone nebula and interpreted it as the most massive and luminous object in NGC 2264. Currently, the object is considered to be a deeply embedded, early-type star lying within a massive molecular core (Dahm 2008). This object is also known as NGC 2264 IRS1 (= C36261 = 2MASS J06411015+0929336, $I_C = 19.068$, $J = 11.508$, $H = 7.643$, $K_s = 4.924$). Allen's source is the brightest mid-IR source in NGC 2264 and is the only object saturated in all short exposure IRAC images. Margulis et al. (1989) obtained the SED slope of the object ($\alpha = +0.1$). Although there are several YSOs around IRS1, the slope measured by Margulis et al. (1989) is unlikely to be affected as Allen's source is one of the brightest objects in the sky in mid-IR and is far brighter than any of the neighboring objects. We consider Allen's source to be a deeply embedded flat spectrum YSO. A very strong, hard X-ray source (EXS-1 = SST 13380, $T_x \approx 100$ MK) lies $11''$ southwest of Allen's source (Simon & Dahm 2005). The object is detected in the short three channels of IRAC and therefore was not classified by its evolutionary stage. If we classify the object in the ([3.6] – [4.5], [4.5] – [5.8]) diagram, EXS-1 is a Class I object.

7.2.5. *The Variability of KH 15D*

One of the more interesting objects in NGC 2264 is KH 15D (= C36305 = SST 13485). KH 15D is very close to IRS1, the brightest IR source in NGC 2264, and the star is on the bright spike of IRS1. It is detected only in channels 1 and 2 of AORs 3956736 and 3957248 (phase = 0.31 of the eclipse light curve;

Hamilton et al. 2005); AORs 3956480 and 3956992 (phase = 0.85 of the eclipse light curve) are on the bright spike and too faint to be measured. In channels 3 and 4, the signal is too weak relative to the brightness of the spike of NGC 2264 IRS1, and therefore could not be measured. Its [3.6] – [4.5] color is slightly red, but not so red as to be classified as a Class II object. Recently, M. Marengo et al. (2009, in preparation) have obtained the light curve of KH 15D in the four IRAC bands, and confirmed that the amplitude in mid-IR wavelengths is the same as that in the optical, which implies that the opacity in the mid-IR is gray, and therefore the size of dust grains in the circumbinary disk around KH 15D is very large (see Herbst et al. 2008).

8. SUMMARY

We have performed mid-IR photometry of the young open cluster NGC 2264 surveyed with the IRAC and MIPS instruments of the *Spitzer Space Telescope*. The results we obtained are summarized as follows.

(1) We presented the *Spitzer* IRAC [3.6], [4.5], [5.8], [8.0], and MIPS [24] data of about 22,000 objects in NGC 2264. We also searched for the optical, near-IR, and X-ray counterparts of all mid-IR sources.

(2) We classified the YSOs in NGC 2264 using two classification schemes—one based on C–C diagrams and the other on the SEDs. We introduced a parameter Q_{CC} in the photometric classification to make full use of the information from multi-color photometry. We also compared the two classifications and found them to be generally consistent with each other.

(3) From the spatial distributions of disked stars (Class I and II objects), we identified two subclustering of Class I objects in the CONE region of Sung et al. (2008). One was the well-known Spokes cluster (Teixeira et al. 2006) and the other was located near the head of the Cone nebula. On the other hand, the S MON region of Sung et al. (2008) mostly comprised Class II objects. These subclustering in NGC 2264 show a distinct difference in the distribution of SED slopes and the mean value of the SED slopes.

(4) We examined the disk fraction of below the PMS locus (BMS) stars and found the fraction with primordial disks to be about 35%. This value is higher than that of normal stars in the PMS locus and supports the idea that BMS stars are young stars with nearly edge-on disks.

(5) We also obtained the result that the fraction of primordial disks increases as the distance from the most massive star S Mon (O7V) increases. This is an important clue that the UV radiation and winds of massive stars affect the fate of primordial disks of nearby low-mass stars.

(6) From a reanalysis of data for young open clusters observed with the *Spitzer Space Telescope*, we found that a common disk lifetime was about 5 Myr, the disk fraction of low-mass stars in NGC 2244 and γ Vel was slightly lower than other clusters with a similar age, and that of η Cha, although the error is large, seems to be higher. This fact implies that the strength of the UV radiation field is one of the most important factors affecting the fate of disks around low-mass stars.

H.S. would like to express his deep thanks to the *Spitzer* Science Center for hosting him as a Visiting Associate for a year. He also thanks J.-E. Lee for valuable suggestions. H.S. acknowledges the support of the Korea Science and Engineering Foundation (KOSEF) to the Astrophysical Research Center for the Structure and Evolution of the Cosmos (ARCSEC²) at Sejong University.

REFERENCES

- Agol, E., Barth, A. J., Wolf, S., & Charbonneau, D. 2004, *ApJ*, **600**, 781
- Allen, D. A. 1972, *ApJ*, **172**, L55
- Allen, L. E., et al. 2004, *ApJS*, **154**, 363
- Allen, L. E., et al. 2007a, *BAAS*, **211**, 8919
- Allen, L. E., et al. 2007b, in *Protostars and Planets V*, ed. B. Reipurth, D. Jewitt, & K. Keli (Tucson, AZ: Univ. Arizona Press), 361
- Aspin, C., & Reipurth, B. 2003, *AJ*, **126**, 2936
- Balog, Z., Muzerolle, J., Rieke, G. H., Su, K. Y. L., Young, E. T., & Megeath, S. T. 2007, *ApJ*, **660**, 1532
- Baraffe, I., Chabrier, G., Allard, F., & Hauschildt, P. H. 1998, *A&A*, **337**, 403
- Bessell, M. S. 1995, in *The Bottom of the Main Sequence and Beyond*, ed. C. Tinney (Berlin: Springer), 123
- Bessell, M. S., Castelli, F., & Plez, B. 1998, *A&A*, **333**, 231
- Briceño, C., Hartmann, L., Hernández, J., Calvet, N., Katherina Vivas, A., Fűrész, G., & Szentesyorgyi, A. 2007, *ApJ*, **661**, 1119
- Carpenter, J. M., Mamajek, E. E., Hillenbrand, L. A., & Meyer, M. R. 2006, *ApJ*, **651**, L49
- Carpenter, J. M., et al. 2009, *ApJS*, **181**, 197
- Chapman, N. L., Mundy, L. G., Lai, S.-P., & Evans, N. J., II. 2009, *ApJ*, **690**, 496
- Cieza, L., & Baliber, N. 2007, *ApJ*, **671**, 605
- Cieza, L., et al. 2007, *ApJ*, **667**, 308
- Dahm, S. E. 2008, in *Handbook of Star Forming Regions*, Vol. 1. The Northern Sky, ed. B. Reipurth (San Francisco, CA: ASP), 966
- Dahm, S. E., & Hillenbrand, L. 2007, *AJ*, **133**, 2072
- Dahm, S. E., & Simon, T. 2005, *AJ*, **129**, 829
- Españillat, C., Calvet, N., Luhman, K. L., Muzerolle, J., & D'Alessio, P. 2008, *ApJ*, **682**, L125
- Evans, N., et al. 2009, arXiv:0901.1691
- Evans, N. J., II, et al. 2003, *PASP*, **115**, 965
- Fazio, G. G., et al. 2004, *ApJS*, **154**, 10
- Fitzpatrick, E. L. 1999, *PASP*, **111**, 63
- Flaccomio, E., Micela, G., & Sciortino, S. 2006, *A&A*, **455**, 903
- Flaherty, K. M., & Muzerolle, J. 2008, *AJ*, **135**, 966
- Fűrész, G., et al. 2006, *ApJ*, **648**, 1090
- Greene, T. P., Wilking, B. A., André, P., Young, E. T., & Lada, C. J. 1994, *ApJ*, **434**, 614
- Gutermuth, R. A., et al. 2008, *ApJ*, **674**, 336
- Haisch, K. E., Jr., Lada, E. A., & Lada, C. J. 2001, *ApJ*, **553**, L153
- Hamilton, C. M., Herbst, W., Shih, C., & Ferro, A. J. 2001, *ApJ*, **554**, L201
- Hamilton, C. M., et al. 2005, *AJ*, **130**, 1896
- Hartmann, L., Megeath, S. T., Allen, L., Luhman, K., Calvet, N., D'Alessio, P., Franco-Hernandez, R., & Fazio, F. 2005, *ApJ*, **629**, 881
- Harvey, P., Merín, B., Huard, T. L., Rebull, L. M., Chapman, N., Evans, N. J., II, & Myers, P. C. 2007, *ApJ*, **663**, 1149
- Harvey, P., et al. 2006, *ApJ*, **644**, 307
- Harvey, P. M., Campbell, M. F., & Hoffmann, W. F. 1977, *ApJ*, **215**, 151
- Hauschildt, P., Allard, F., & Baron, E. 1999, *ApJ*, **512**, 377
- Herbig, G. H. 1954, *ApJ*, **119**, 483
- Herbig, G. H. 1962, *ApJ*, **135**, 736
- Herbst, W., Hamilton, C. M., LeDuc, K., Winn, J. N., Johns-Krull, C. M., Mundt, R., & Ibrahimov, M. 2008, *Nature*, **452**, 194
- Hernández, J., Hartmann, L., Calvet, N., Jeffries, R. D., Gutermuth, R., Muzerolle, J., & Stauffer, J. 2008, *ApJ*, **686**, 1195
- Hernández, J., et al. 2007a, *ApJ*, **662**, 1067
- Hernández, J., et al. 2007b, *ApJ*, **671**, 1784
- Hora, J. L., et al. 2008, *PASP*, **120**, 1233
- Indebetouw, R., et al. 2005, *ApJ*, **619**, 931
- Jeffries, R. D., Naylor, T., Walter, F. M., Pozzo, M. P., & Devey, C. R. 2009, *MNRAS*, **393**, 538
- Keller, L. D., et al. 2008, *ApJ*, **684**, 411
- Lada, C. J. 1987, in *IAU Symp. 115*, *Star Forming Regions*, ed. M. Peimbert & J. Jugaku (Dordrecht: Reidel), 1
- Lada, C. J., & Wilking, B. A. 1984, *ApJ*, **287**, 610
- Lada, C. J., et al. 2006, *AJ*, **131**, 1574
- Lada, H. J., Young, E. T., & Greene, T. P. 1993, *ApJ*, **408**, 471
- Luhman, K. L., & Steeghs, D. 2004, *ApJ*, **609**, 917
- Lynden-Bell, D., & Pringle, J. E. 1974, *MNRAS*, **168**, 603
- Margulis, M., Lada, C. J., & Young, E. T. 1989, *ApJ*, **345**, 906
- Megeath, S. T., Hartmann, L., Luhman, K. L., & Fazio, G. G. 2005, *ApJ*, **634**, L113
- Megeath, S. T., et al. 2004, *ApJS*, **154**, 367
- Morales-Calderon, M., et al. 2008, *ApJ*, submitted (arXiv:0907.3360)
- O'Dell, C. R., & Wen, Z. 1994, *ApJ*, **436**, 194
- Ogura, K. 1984, *PASJ*, **36**, 139
- Padgett, D. L., et al. 2006, *ApJ*, **645**, 1283
- Padgett, D. L., et al. 2007, *BAAS*, **211**, 2904
- Palla, F., & Stahler, S. 2002, *ApJ*, **581**, 1194
- Park, B.-G., & Sung, H. 2002, *AJ*, **123**, 892
- Park, B.-G., Sung, H., & Kang, Y. H. 2001, *J. Korean Astron. Soc.*, **34**, 149
- Pérez, M. R., McCollum, B., van den Ancker, M. E., & Jøner, M. D. 2008, *A&A*, **486**, 533
- Ramírez, S. V., et al. 2004, *AJ*, **127**, 2659
- Rebull, L. M., et al. 2002, *AJ*, **123**, 1528
- Rebull, L. M., et al. 2007, *ApJS*, **171**, 447
- Reipurth, B., Pettersson, B., Armond, T., Bally, J., & Vaz, L. P. R. 2004, *AJ*, **127**, 1117
- Rieke, et al. 2004, *ApJS*, **154**, 25
- Robitaille, T. P., et al. 2007, *ApJS*, **169**, 328
- Sicilia-Aguilar, A., Hartmann, L., Fűrész, G., Henning, T., Dullemond, C., & Brandner, W. 2006, *AJ*, **132**, 2135
- Sicilia-Aguilar, A., Hartmann, L., Hernández, J., Briceño, C., & Calvet, N. 2005, *AJ*, **130**, 188
- Siess, L., Dufour, E., & Forestini, M. 2000, *A&A*, **358**, 593
- Simon, T., & Dahm, S. E. 2005, *ApJ*, **618**, 795
- Skrutskie, M. F., et al. 2006, *AJ*, **131**, 1163
- Slesnick, C. L., Hillenbrand, L. A., & Carpenter, J. M. 2004, *ApJ*, **610**, 1045
- Stern, D., et al. 2005, *ApJ*, **631**, 163
- Strom, K. M., Strom, S. E., Edwards, S., Cabrit, N., & Skrutskie, M. F. 1989, *AJ*, **97**, 1451
- Strom, K. M., Strom, S. E., & Yost, J. 1971, *ApJ*, **165**, 479
- Strom, K. M., Strom, S. E., Yost, J., Carrasco, L., & Grasdalen, G. 1972, *ApJ*, **173**, 353
- Sung, H., Bessell, M. S., & Chun, M.-Y. 2004, *AJ*, **128**, 1684
- Sung, H., Bessell, M. S., Chun, M.-Y., Karimov, R., & Ibrahimov, M. 2008, *AJ*, **135**, 441
- Sung, H., Bessell, M. S., & Lee, S.-W. 1997, *AJ*, **114**, 2644
- Sung, H., & Lee, S.-W. 1995, *J. Korean Astron. Soc.*, **28**, 119
- Sung, H., et al. 2007, *RevMexAA Conf. Ser.* **28**, 113
- Teixeira, P. S., et al. 2006, *ApJ*, **636**, L45
- Vijh, U. P., et al. 2008, *AJ*, **137**, 3139
- Wang, J., et al. 2008, *ApJ*, **675**, 464
- Weingartner, J. C., & Draine, B. T. 2001, *ApJ*, **548**, 296
- Winston, E., et al. 2007, *ApJ*, **669**, 493
- Young, E. T., et al. 2006, *ApJ*, **642**, 972